The Cryosphere Discuss., doi:10.5194/tc-2016-156, 2016
Manuscript under review for journal The Cryosphere
Published: 7 July 2016

The Cryosphere Discussions
Open Access
EGU

Sonar Gas Flux Estimation by Bubble Insonification: Application to Methane Bubble Fluxes from the East Siberian Arctic Shelf Seabed

Ira Leifer[1], Denis Chernykh[2,3], Natalia Shakhova[3,4], Igor Semiletov[2,3,4]

[1] Bubbleology Research International, Solvang, CA 93463

[2] Russian Academy of Science, Pacific Oceanological Institute, Vladivostok, Russia

[3] National Tomsk Research Polytechnic University, Tomsk, Russia

[4] University Alaska Fairbanks, International Arctic Research Center, Fairbanks, USA

Abstract

Sonar surveys provide an effective mechanism for mapping seabed methane flux emissions, with Arctic submerged permafrost seepage having great potential to significantly affect climate. We created *in situ* engineered bubble plumes from 40-m depth with fluxes spanning 0.019 to 1.1 L/s to derive the *in situ* calibration curve, $Q(\sigma)$. Non-linear curves relating flux, Q, to sonar return, s, for a multibeam echosounder (MBES) and a single beam echosounder (SBES) for a range of depths demonstrated significant bubble-bubble acoustic interactions – precluding the use of a theoretical calibration function, $Q(\sigma)$, wherein bubble $\sigma(r)$ scales with the radius, r, size distribution. Bubble plume sonar occurrence, $\Psi(\sigma)$, with respect to Q found $\Psi(\sigma)$ for weak σ well described by a power law that likely correlated with small bubble dispersion and strongly depth dependent. $\Psi(\sigma)$ for strong s largely was depth-independent, consistent with bubble plume behavior where large bubbles in a plume remain in a focused core. As a result, $\Psi(\sigma)$ was bimodal for all but the weakest plumes.

$\Psi(\sigma)$ was applied to sonar observations of natural arctic Laptev Sea, seepage including accounting for volumetric change with a numerical bubble plume. Based on MBES data, values of total Q_m, the mass flux, were 5.56, 42.73, and 4.88 mmol/s with good to reasonable agreement between the SBES and MBES data (4-37%) for total Q. Seepage occurrence, $\Psi(Q)$, was bimodal, with weak $\Psi(Q)$ in each seep area well described by a power law, suggesting primarily minor bubble plumes. Seepage mapped spatial patterns suggested subsurface geologic control attributing methane fluxes to the current state of subsea permafrost.

Keywords: Bubble, multibeam sonar, single beam, quantification, Arctic, methane, submerged permafrost, field study, seep, engineered bubble plume

The Cryosphere Discuss., doi:10.5194/tc-2016-156, 2016
Manuscript under review for journal The Cryosphere
Published: 7 July 2016

1. Introduction

1.1 Arctic methane and climate change

Methane and Arctic climate change

The second-most important anthropogenic greenhouse gas on a century timescale after carbon dioxide, CO_2 is methane, CH_4, (Forster et al. 2007); however, on decadal time scales comparable to its atmospheric lifetime, CH_4 is more important to the atmospheric radiative balance than CO_2 (IPCC, 2007; Fig 2.21). After nearly stabilizing, atmospheric concentrations began increasing a decade ago, although the underlying reasons remain poorly understood (Nisbet et al., 2014). Despite likely increasing future natural emissions from global warming feedbacks (Rigby et al., 2008) and anthropogenic activities (Kirschke et al., 2013; Wunch et al., 2009), many current source estimates have large uncertainties with greater uncertainty in future trends, particularly in the Arctic.

Currently, Arctic global warming is the strongest, termed Arctic amplification (Graversen et al., 2008). Permafrost CH_4 provides an important feedback, where warming Arctic temperatures release CH_4 sequestered in and under terrestrial (Friedlingstein et al., 2006; Lemke et al., 2007) and sub-sea permafrost, which is submerged terrestrial permafrost (Shakhova and Semiletov, 2009). Sediment accumulation rates for the Arctic continental shelf are 5 times greater than elsewhere in the World's Oceans. For example, sedimentation for the Siberian Arctic shelf where the six Great Siberian Rivers outflow, has deposited organic carbon into bottom sediments that approximately equals accumulations over the entire pelagic area of the World's Oceans. This leads to the thickest (up to 20 km) and most extensive sedimentary basin in the world, the "Arctic super carbon pool" (Gramberg et al., 1983).

The Siberian Arctic Shelf

The Siberian Arctic Shelf subsea permafrost, CH_4 hydrates, and natural gas systems contains vast CH_4 deposits (Gautier et al., 2009; Gramberg et al., 1983; Romanovskii et al., 2005; Serreze et al., 2009; Shakhova et al., 2009a, 2010a; 2010b) of which a large fraction is CH_4 hydrate deposits (Makogon et al., 2007; Soloviev et al., 1987). According to Dickens (2003), subsea continental shelf reservoirs are estimated to contain about 10,000 gigatonnes Gt (1 Gt=10^{15}g) of CH_4 hydrates, compared to terrestrial permafrost, which is estimated at 400 Gt of CH_4 hydrates. The Arctic continental shelf makes up 25% of the entire area of the world's oceanic continental shelves (7 million km^2 of the ocean's area, 28.8 million km^2) and is estimated to contain 2,500 Gt of carbon in the form of CH_4 hydrates. This is more than 3 times greater than the amount of carbon currently stored in the atmosphere and ~500 times greater than the current atmospheric CH_4 reservoir (IPCC, 2007). Remobilization of only a small fraction of CH_4 in these deposits could trigger abrupt climate warming; for example, Archer and Buffett (2005) estimated

The Cryosphere Discuss., doi:10.5194/tc-2016-156, 2016
Manuscript under review for journal The Cryosphere
Published: 7 July 2016

that release to the atmosphere of just 0.5% of the CH_4 in Arctic shelf hydrates could cause abrupt climate change.

The East Siberian Arctic Shelf (ESAS) is the world's largest and shallowest shelf (covering $2.1x10^6$ km^2) containing the largest area of submerged permafrost by far (Shakhova et al., 2010a, b). The ESAS is a seaward extension of the Siberian tundra that was flooded during the Holocene transgression, 7-15 kyr ago (Romanovskii et al., 2005). The ESAS comprises ~25% of the Arctic continental shelf and contains over 80% of existing subsea permafrost and shallow hydrate deposits, estimated at ~1400 Gt carbon (Shakhova et al., 2010a). This reservoir includes ESAS hydrate deposits, estimated at ~540 Gt of CH_4, with an additional 2/3 (~360 Gt) trapped below as free gas (Gramberg et al., 1983; Soloviev et al., 1987). ESAS subsea permafrost is Siberian terrestrial permafrost that was submerged and thus is expected to contain similar permafrost organic carbon (OC) deposits to terrestrial, implying a further 500 OC Gt within an ~25-m thick permafrost layer. Thus, ESAS carbon stores are comparable to the Arctic soil carbon pool, which includes tundra and taiga (~1000 Gt C) and coastal permafrost (~400 Gt C) (Tarnocai et al., 2009).

The ESAS subsea permafrost is changing in response to glacial/interglacial Arctic warming (~7°C), and warming from the overlying seawater (~10°C) since inundation in the early Holocene, with additional ESAS seawater warming in recent decades (Biastoch et al., 2011; Nicolsky et al., 2012; Semiletov et al., 2012, 2013;Shakhova et al., 2014). The Siberian rivers transport additional heat to the Arctic shelf which results from terrestrial ecosystem responses to global warming. This includes the degradation of terrestrial permafrost and increased river runoff, which warms shelf waters. In turn, this warm runoff drives a downward heat flux to shelf sediments and sub-sea permafrost (Shakhova and Semiletov, 2007; Shakhova et al., 2014). Also, there is the potential for abrupt CH_4 release on the ESAS and its continental slope related to temperature destabilization of Arctic shallow and oceanic hydrates. The extent of the ESAS gas hydrate stability zone is expected to be highly sensitive to small temperature changes (Dickens, 2003).

Permafrost Degradation

Subsea permafrost is an impermeable lid (where continuous) preventing the upward migration of CH_4 and other geological fluids, hence the great concern for its degradation and sub sequent release of sequestered CH_4 to the shallow ocean and then atmosphere. Both onshore and offshore Arctic permafrost degrade from two directions (Ostercamp, 2001; Shakhova and Semiletov, 2009). Thawing occurs from the top downward, where the active layer expands downward creating taliks (bodies of thawed permafrost). Permafrost also degrades from the bottom up as a result of geothermal heat flux, where heat from the Earth's interior flows upward, thawing frozen sediments from below. The latter only has a significant

The Cryosphere Discuss., doi:10.5194/tc-2016-156, 2016
Manuscript under review for journal The Cryosphere
Published: 7 July 2016

93 effect for submerged offshore permafrost (Romanovskii et al., 2005), because the high Arctic terrestrial
94 permafrost is thick and continuous, allowing its bottom to absorb upward heat flows with negligible
95 effect. For example, an offshore permafrost sediment core (obtained by authors' team from the fast ice in
96 April 2011 to 57 m below the Laptev sea floor) was unfrozen and 8-12°C warmer than a core recovered
97 from the Lena Delta' borehole (Shakhova et al., 2014).

98 Recent studies have identified four main subsea permafrost degradation mechanisms, which provide
99 geologic control of the thermal state of subsea permafrost and also hydrate stability. The most important,
100 which operates on long (millennia) timescales, is the increasing temperature of the overlying bottom
101 seawater and the duration of its interaction with the permafrost both by heat transfer and salinization
102 (Soloviev et al., 1987; Shakhova et al., 2014, 2015). A second process that provides geologic control
103 arises from heating from large Siberian rivers which drives bottom water warming and is proposed to
104 control the distribution of open taliks in coastal ESAS waters (Shakhova et al., 2014). Thirdly, high
105 geothermal heat flow in rift zones induces fractures that provide geologic control (Drachev et al., 2003;
106 Nicolsky et al., 2012). Finally, areas of high heat flow includes relic–thaw lakes and river-valleys that
107 were submerged during the Holocene inundation, but still drive modern permafrost degradation (Nicolsky
108 and Shaklhova, 2010; Nicolsky et al., 2012; Shakhova et al., 2009b, c).

109 Subsea permafrost degradation is greatest in the outer shelf waters, which are deeper than 50 m, where
110 submergence at the beginning of Holocene (~10-15 thousands years ago) first occurred (Bauch et al.,
111 2001) and where4 current models predict discontinuous and mostly degraded permafrost in the outer
112 Laptev Sea. The formation and growth of subsea thaw lakes also likely is greater where riverine heat
113 inputs combines synergistically with longer permafrost submergence (Shakhova and Semiletov, 2007;
114 Holemann et al., 2011; Shakhova et al., 2014). This also leads to the evolution and growth of taliks, which
115 provide effective gas migration pathways to the shallow waters of the ESAS (Nicolsky and Shakhova,
116 2010; Shakhova et al., 2009b, 2014, 2015; Nicolsky et al., 2012). River outflow also affects ocean
117 temperatures by introducing colored dissolved organic matter (CDOM), which concentrates absorption of
118 solar radiation in near surface waters, accelerating ocean warming, freshening, and acidification (Pugach
119 et al., 2015; Semiletov et al., 2013, 2016).

120 Geologic heat flow is strong in the Laptev Sea (85-117 m W m^{-2}) where active seafloor spreading is
121 converting into continental rifting. In fact, the northern Laptev Sea also is one of the few places where
122 active oceanic spreading approaches a continental margin (Drachev et al., 2003) and correlates with the
123 "hot" area crossed by the Ust' Lensky Rift and Khatanga-Lomonosov Fracture (Drachev et al., 2003;
124 Nicolsky et al., 2012). Evidence for this rifting is provided by hydrothermal fauna remnants documented

The Cryosphere Discuss., doi:10.5194/tc-2016-156, 2016
Manuscript under review for journal The Cryosphere
Published: 7 July 2016

around grabens (dropped blocks between faults) in the up-slope area that typically occur along oceanic divergent axes (Drachev et al., 2003). Grabens in the ESAS often manifest as linear structures and also often correlate spatially with paleo-river valleys.

Migration from this submerged permafrost reservoir to the seabed feeds a vast marine seep field entirely in shallow waters, where emissions contribute directly to the atmospheric budget (Shakhova et al., 2014). At-sea observations show dissolved CH_4 supersaturation with respect to the atmosphere for >80% of ESAS bottom waters and >50% of surface waters (Shakhova et al., 2010a, 2010b). This seepage is almost entirely ancient CH_4 – modern CH_4 production from old OC is negligible based on recent microbiological studies (2011-2012) in ESAS surface and long-sediment cores (V. Samarkin, unpublished data). Indeed, in the ESAS, sediment OC content varies by a factor of ~4, while ebullition CH_4 fluxes vary by orders of magnitude (Shakhova et al., 2015).

1.2 Study motivation

Given the extent of Arctic seepage and the magnitude of current and potential future emissions, there is a critical need for new approaches to effectively, rapidly, and quantitatively survey large seepage areas. Video is inadequate to survey extensive or widely dispersed seepage, a task for which sonar (active acoustics) excels. This study's motivation is to demonstrate an improved approach for seabed seepage survey in the Arctic, using *in situ calibrated* sonar-derived bubble fluxes.

Herein, we present *in situ* calibration experiments in the ESAS to investigate the evolution of bubble plume sonar return (multiple beam echosounder–MBES and single beam echosounder–SBES) from rising engineered bubble plumes spanning a broad range of flow rates covering typical seepage bubble flows to infer the relative importance of small and large bubbles to sonar return signatures. Analysis demonstrated that bubble-bubble acoustic interactions are *non-negligible* for the first 15 m of rise at least, preventing simple flux inversion by dividing total sonar return by the sum of individual bubble sonar cross sections for an assumed bubble size or size distribution.

The calibration curves then were applied to quantify *in situ* sonar observations of three areas of active natural bubble seepage nearby the site of the calibration experiments. Because the calibration and seep bubble plumes were different gases and from different water depths, with slightly different temperature profiles, bubble dissolution rates are different – i.e., for the same seabed mean volume flux, the depth-window-averaged volume fluxes are different. We make a first attempt to correct for this factor by applying a numerical bubble-plume model initialized with a typical seep bubble plume size distribution to the two bubble flows (calibration and natural seepage).

The Cryosphere Discuss., doi:10.5194/tc-2016-156, 2016
Manuscript under review for journal The Cryosphere
Published: 7 July 2016

1.3. Marine seepage

Marine seepage is a global phenomena where CH_4 and other trace components escape as bubbles from the seabed and rise towards the sea surface (Judd and Hovland, 2009), dissolving and depositing CH_4 in the water column while transporting their remaining contents to the sea surface – if they do not dissolve subsurface (Leifer and Patro, 2002b).

In the shallow waters, like the Coal Oil Point (COP) seep field, most of the CH_4 reaches the atmosphere directly (Clark et al., 2005) from mixing in the near field (Clark et al., 2000) and in the far (down-current) field when winds strengthen as typical occurs diurnally in coastal California. The ultimate fate of dissolved seep CH_4 depends most strongly on its deposition depth (Solomon et al., 2009) with CH_4 below the Winter Wave Mixed Layer (WWML) largely being oxidized microbially (Rehder et al., 1999). However, even for deepsea seepage (to ~1 km), field studies show seep bubble-plume transport of CH_4 to the upper water-column and atmosphere (MacDonald, 2011) due to plume processes (Leifer et al., 2009) and hydrate skin phenomena (Rehder et al., 2009; Warzinski et al., 2014). Still for deepsea seepage, a significant fraction of seabed CH_4 emissions are deposited below the WWML where they are oxidized microbially. In the shallow ESAS, virtually all the seabed CH_4 (dissolved and gaseous) is emitted in the WWML and escapes to the atmosphere (Shakhova et al., 2014). However, even CH_4 dissolved below the Arctic WWML is less likely to be oxidized than in non-Arctic waters because Arctic CH_4 oxidation rates are very slow, 300-1000 days (Shakhova et al., 2015). These slower rates allow release of some of this deeper aqueous inventory to the atmosphere during storms and fall-winter convection (Shakhova et al., 2010a, 2014).

Plume processes are important. Several factors control the fate of seep bubble CH_4 including depth, bubble size, plume volume flux (Leifer et al., 2006; Leifer and Patro, 2002b), and the vertical bubble velocity, V_{up}, which includes the upwelling flow and depends on the plume volume flux (Leifer, 2010; Leifer et al., 2009). Another documented important plume process is enhanced aqueous concentrations relative to the surrounding water, which enhances bubble survival (Leifer et al., 2006).

1.3 Seep Bubble Measurements

Currently, natural seepage bubble-plume size distributions, Φ, have only been measured by video and passive acoustics (Leifer, 2010), with the latter demonstrated only for low-emission-rate bubble plumes where the individual bubbles acoustic signatures can be identified (Leifer and Tang, 2007). Although highly accurate, video requires significant power, data storage, and its analysis is complex; nor is it a remote sensing technique (Leifer, 2010)–i.e., currents shift bubbles out of the measurement volume.

The Cryosphere Discuss., doi:10.5194/tc-2016-156, 2016
Manuscript under review for journal The Cryosphere
Published: 7 July 2016

187 Most natural seepage bubbles fall within a relatively narrow size range. Specifically, based on a review of
188 39 bubble-plume size distributions (the most comprehensive to date), Leifer (2010) found that the vast
189 majority of seep bubble plumes could be classified in two primary categories, termed major and minor,
190 with the latter most common, a characterization found in other studies, reviewed in Leifer (2010).
191 Φ for minor bubble plumes are well described by a Gaussian function and comprised of bubbles largely in
192 a narrow size range, $1000 < r_e < 4000$ µm, where r_e is the equivalent spherical radius. Major bubble
193 plumes generally escape from higher flow vents as a fragmenting gas jet with a power law size
194 distribution. Most major bubble plumes are small; however most of the plume volume is transported by
195 the largest bubbles, up to $r \sim 1$ cm.

196 Video bubble measurement is highly local and thus a poor survey (or monitoring) tool. A hybrid ROV
197 video approach was demonstrated by Leifer (2015) for an 1100 m^2 North Sea seep site where the ROV
198 was flown in a grid pattern. A total of 176 bubble plumes were classified by appearance and assigned an
199 emission flow, which was integrated for the entire site (estimated at 440 plumes), with the strongest
200 plume class's flux measured directly in the field. The video survey required about a full day of ROV dive
201 time and analysis was labor intensive.

202 **1.4 Sonar Seep Bubble Measurements**

203 Reported seepage areas span a large range of spatial areas and number of plumes. Sonar has been used to
204 survey concentrated seep area covering ~1000 m^2 in the North Sea noted above (Schneider von Deimling
205 et al., 2010; Wilson et al., 2015), and far more dispersed and weaker seepage in the Black Sea of ~2500
206 plume in an areas of ~20 km^2 (Greinert et al., 2010). Significantly larger and stronger seepage in the COP
207 seep field, offshore California have been mapped by sonar too. The COP seep field covers ~3 km^2 of
208 active seabed in an 18 km^2 area (Hornafius et al., 1999), and comprises tens of thousands of plumes. The
209 COP seep field includes highly focused seepage, termed megaseeps, which release more than a million
210 liters per day (Washburn et al., 2005). Megaseeps may arise from dozens to thousands of vents. Seepage
211 on far larger scale exists in the ESAS where ~30,000 plumes were identified manually in just two
212 transects. Seepage densities as high as ~3000 seep bubble plumes per km^2 were found transecting a single
213 hotspot. Based on the hotspot size (18,400 km^2), an order of magnitude estimate suggests 60 million seep
214 plumes in the hotspot alone. While sonar surveys of a localized site, e.g., the North Sea site, can be
215 conducted in a few minutes, the ESAS sonar survey required a month for two transects (Stubbs, 2010;
216 Shakhova et al., 2014).

217 Sonar is highly effective at seep emission mapping; however interpretation challenges exist even for
218 qualitatively assessment of relative emission strength. For SBES systems, there is geometric uncertainty –

The Cryosphere Discuss., doi:10.5194/tc-2016-156, 2016
Manuscript under review for journal The Cryosphere
Published: 7 July 2016

219 the plume's angular location is unknown; a problem resolved by MBES systems (Leifer et al., 2010). In
220 addition, sonar (SBES or MBES) loses fidelity from multiple plumes in close proximity (Schneider von
221 Deimling et al., 2011; Wilson et al., 2015) where the sonar returns along multiple pathways, creating
222 ghosts, shadow noise, off-beam returns, scattering loss, and other artifacts (Wilson et al., 2015). Note, if
223 bubble spatial densities are sufficiently high for artifacts to occur between plumes, then they are
224 sufficiently high to produce artifacts within plumes between individual bubbles. For very high flux bubble
225 plumes, the sonar return signal can be largely or even completely lost (Leifer et al., 2010). In addition, the
226 vessel's acoustic environment can be challenging both acoustically and from electrical noise.
227 Furthermore, the ocean is far from acoustically transparent, with signal loss and scattering from
228 suspended sediment and biota, often in layers, as well as other marine acoustic features.

229 Although seemingly straightforward, there are many challenges to quantitative derivation of bubble
230 emission flux from sonar return, which at its basis relates to the interaction of sound with a bubble. For a
231 single spherical bubble the relationship has long been known, with resonance given by the Minnaert
232 (1933) equation:

233 $$f_o = \frac{1}{2\pi r}\left(\frac{3\gamma P}{\rho}\right)^{1/2} \quad (1)$$

234 where f_o is the resonance (or Minnaert) frequency, γ is the resonance (or Minnaert) frequency, P is
235 pressure, and ρ is pressure, and for Minna non-spherical bubbles (r > 150 µm) an eccentricity correction
236 is needed to account for the angle between the bubble axes and the sound wave front. Bubble
237 eccentricities vary from 1.0 for spherical bubbles to 2 or greater for r > 3500 µm (Clift et al., 1978). For a
238 single spherical bubble, the back-scattering cross section, σ_B, near f_o is (Weber et al., 2014):

239 $$\sigma_B = \frac{r^2}{\left[\left(\frac{f_o}{f}\right)^2 - 1\right]^2 + \delta^2} \quad (2)$$

240 where f is frequency and δ is the damping term that can be approximated as $\delta \sim 0.03 f^{0.3}$ with f in kHz.
241 From, here, integrating over the bubble emission size distribution, $\Phi(r)$, which is the number of bubbles
242 in a radius bin, r, passing through the measurement plane, combined with $V_Z(r)$, the bubble vertical
243 velocity, which is a function of r, over the measurement volume yields the total plume cross-section if
244 bubbles are acoustically non-interactive and scattering is isotropic.

245 .

The Cryosphere Discuss., doi:10.5194/tc-2016-156, 2016
Manuscript under review for journal The Cryosphere
Published: 7 July 2016

Scattering is radially symmetric about the plume axis, θ, but not in the azimuth, β. Thus, for ellipsoidal bubbles in a bubble plume observed from angle β, the scattered power, P_{Bs}, is

$$P_{bs}(\beta) = \iiint_{x,y,r} \sigma_B(\beta)\Phi(x,y,z,r_e) + \iiint_{x,y,r,k,m} G_{k.m}\sigma_{k.m} \quad (3)$$

where k and m are indices of different bubbles ($k \neq m$) and $\Phi(r,z)$ changes with altitude above the seabed due to dissolution and air uptake, and can vary horizontally with position in the plume due to currents and the complex fluid motions associated with bubble plumes (Asaeda and Imberger, 1993; Leifer et al., 2009). The equation includes a second acoustic interaction term and is the integral over $bubble_k$-$bubble_m$ interactions (multiple scattering and acoustic coupling). This term is described by the interaction function, G, and depends on the bubble sizes, separation distance and angle, etc. In the case of a sufficiently dispersed bubble plume (large bubble-bubble separation), $G_{k,m}=0$ and bubbles are acoustically non-interacting.

In most seep bubble plumes, the close proximity between bubbles creates bubble-bubble acoustic interactions through acoustic coupling and/or multiple scattering. Multiple scattering occurs when the sound scattered from one bubble interacts and scatters from a second bubble back in the direction of the sonar receiver. The significance of multiple scattering is provided by artifacts like ghosting between plumes (not return from the sonar beam sidelobes).

Acoustic coupling occurs for bubbles within 10-20 bubble radii of each other, i.e., a few centimeters, such that the water surrounding the bubble no longer is incompressible, leading to a frequency shift (Leifer and Tang, 2007). Because sonar is spectrally selective, frequency shifts from acoustic coupling can decrease the sonar return signal. In most seep bubble plumes, acoustic coupling should be small except very near the seabed where bubbles still rise in close proximity, or where bubbles rise in dense clumps. In the latter case, smaller bubbles often draft larger bubbles and remain in close proximity (Tsuchiya et al., 1996).

2. Methodology

2.1. Coal Oil Point seep field Scoping Study

A precursor study was conducted in the COP seep field (Fig. 1) prior to the Arctic field experiment to demonstrate 4D seep monitoring by a scanning MBES. The rotator-lander was deployed ~15 m from the center of Shane Seep, which covers an area of ~10^4 m^2 in ~20-m water depth and comprises on the order of 1000 individual vents or bubble plumes (Fig. 1B).

The Cryosphere Discuss., doi:10.5194/tc-2016-156, 2016
Manuscript under review for journal The Cryosphere
Published: 7 July 2016

274 The lander included a MBES (DeltaT, Imagenex, Vancouver, Canada) and compass (Ocean Server, MA)
275 on an underwater rotator (Sidus Solutions, CA) with azimuthal rotation of up to 270° angle range. The
276 sonar produced a vertically oriented 128-beam fan spanning 120°, tilted upwards to reduce seabed
277 backscatter. Two *in situ* calibration air bubble flows were deployed ~8 m from the lander at azimuthal
278 angles beyond the active seepage area and were traversed during each sonar rotation cycle. Regulated
279 airflow from an onboard compressor fed these bubble plumes and was measured by two rotameters.

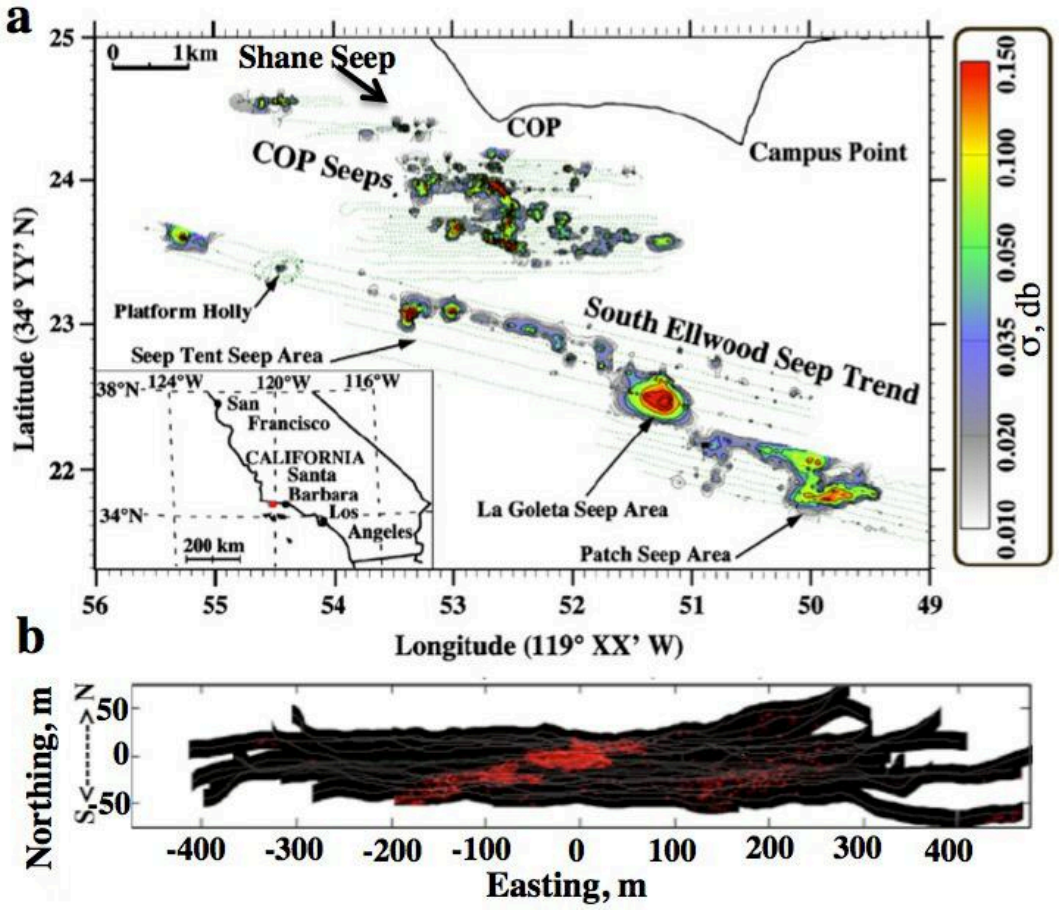

280

281 **Figure 1. a.** Coal Oil Point (COP) seep field map, showing Shane Seep location where the scoping study
282 was performed based on 2005 sonar data. From Leifer et al. (2010). **b.** Multibeam sonar survey map (2-m
283 depth window at a seabed-following height of 4 m) of Shane Seep in the COP seep field, collected in
284 2009.

The Cryosphere Discuss., doi:10.5194/tc-2016-156, 2016
Manuscript under review for journal The Cryosphere
Published: 7 July 2016

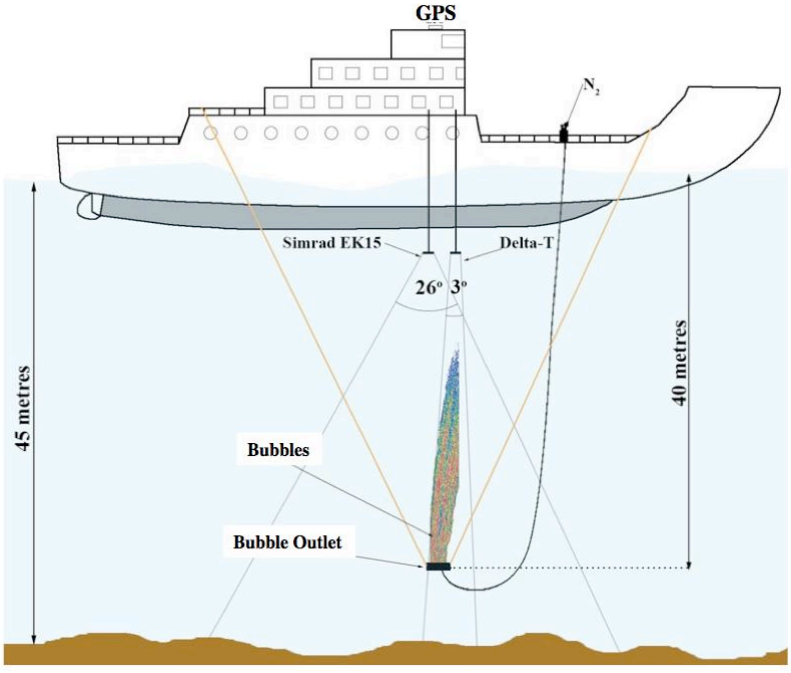

Figure 2. *In situ* calibration experiment set up schematic as deployed in the ESAS.

2.2. Arctic Calibration Experimental Set-up

For the control sonar bubble plume study, bubble plumes were made from nitrogen supplied by a pressure tank on the vessel foredeck. A 70-m long, 12-mm diameter, 6-mm wall thickness, air supply tubing was attached by a Kevlar rope to a heavy metal weight (~30 kg) that ballasted against buoyancy of air in the tubing and drag from currents. The supply tube was deployed to 40-m depth in water of ~45-m depth (Fig. 5) and the rising bubble plume was observed with MBES and SBES. The sonars were located near each other so that their beam coverage overlapped with the center beam focused on the end of the bubble stream. Bubbles were produced from a 4-mm diameter copper nozzle attached at the end of the air supply tube.

Gas flow was controlled using standard flow meters, one port of which was connected to a PVC tube and another was connected to a 2-way valve, the second port of which was connected to the gas tank through the gas manifold. The manifold consisted of a high-pressure sensor of the tank pressure and a low-pressure sensor for the out-coming pressure (5.5 bar). We used temperature-compensated differential pressure sensors with a manufacturer-specified range of ±1 psi (equivalent to ±70 cm of water). The sensor has manufacturer-specified accuracy and stability of ±0.5% FSD (full scale deflection over the operating pressure range of the sensor over 1 yr, between 0 and 50°C) and repeatability errors of ±0.25%

The Cryosphere Discuss., doi:10.5194/tc-2016-156, 2016
Manuscript under review for journal The Cryosphere
Published: 7 July 2016

303 FSD. For the study, the gas flow was varied from 0.5 to 150 L min^{-1} at 5.5 bar (equal to the bubble outlet
304 hydrostatic pressure). For each experiment, the gas flow was allowed to stabilize and then sonar data were
305 recorded for ~10 minutes.

306 SBES bubble plume data were collected by a SIMRAD EK15 SW 1.0.0 echosounder (www.simrad.com)
307 at 200 kHz, with a 1 ms pulse duration at 10 Hz, 26° beam width, and built-in calibration system. MBES
308 bubble plume data were collected by a DeltaT Profiler (Imagenex, British Columbia, Canada) at 260 kHz.
309 Sonar data including seep bubble plumes were recorded at an average survey speed of 4-6 knots. Sonar
310 backscatter was calibrated using acoustic targets (SIMRAD, Denmark). Initial data visualization and
311 processing used EchoView and Sonar5 software (SIMRAD), for the EK15.

312 **2.2 Arctic Field Campaign**

313 Field data were obtained during an expedition onboard the research vessel R/V *Victor Buynitsky* from 2
314 Sept. to 3 Oct. 2012 (Figs. 3 and 4). The R/V *Victor Buynitsky sailed* from Murmansk to the Laptev Sea
315 and the adjacent portion of the ESAS. The weather during the expedition was typical for this region for
316 this time of the year (3-4 storm events with wind speed >10 m s^{-1}). The calibration experiment was
317 performed in the Kara Sea for 45-m water depths under favorable weather: calm sea with wind speed 3-5
318 m s^{-1} and wave height of 0.2-0.5 m. The expedition's overarching goal was to improve understanding of
319 the current scale of ESAS CH_4 emissions in order to develop a conceptual model of CH_4 propagation from
320 the seabed to the atmosphere, including assessing source strengths and their dynamics.

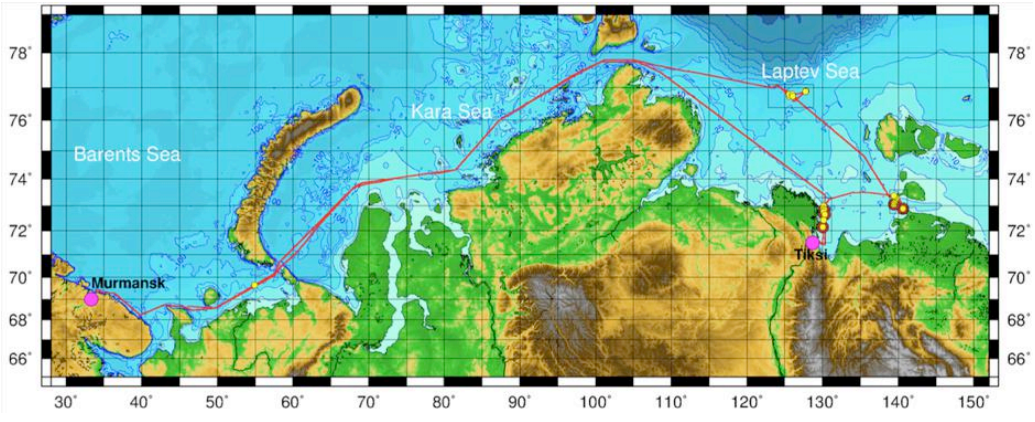

321
322 **Figure 3.** Map for R/V *Victor Buynitsky* cruise, 2012.

The Cryosphere Discuss., doi:10.5194/tc-2016-156, 2016
Manuscript under review for journal The Cryosphere
Published: 7 July 2016

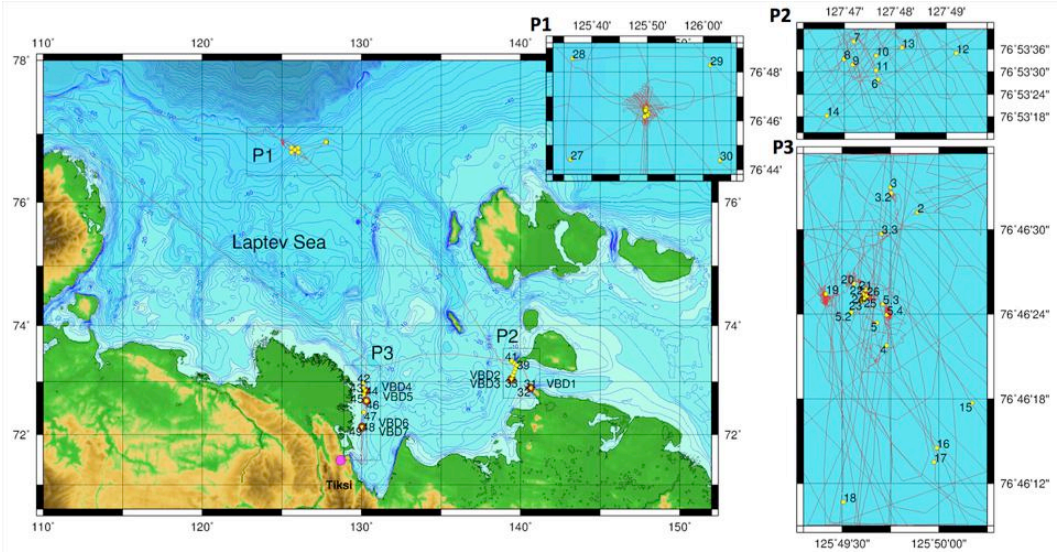

Figure 4. Locations of oceanographic stations for RV *Victor Buynitsky* cruise, 2012, marked by yellow circles. Polygons of major focus areas are marked as P1 (northern Laptev Sea), P2 (east Lena Delta) and P3 (Dmitry Laptev Strait), shown in insets. Ship tracks accompanied by CTD measurements (and geophysical survey) performed in the P1 are shown as red lines.

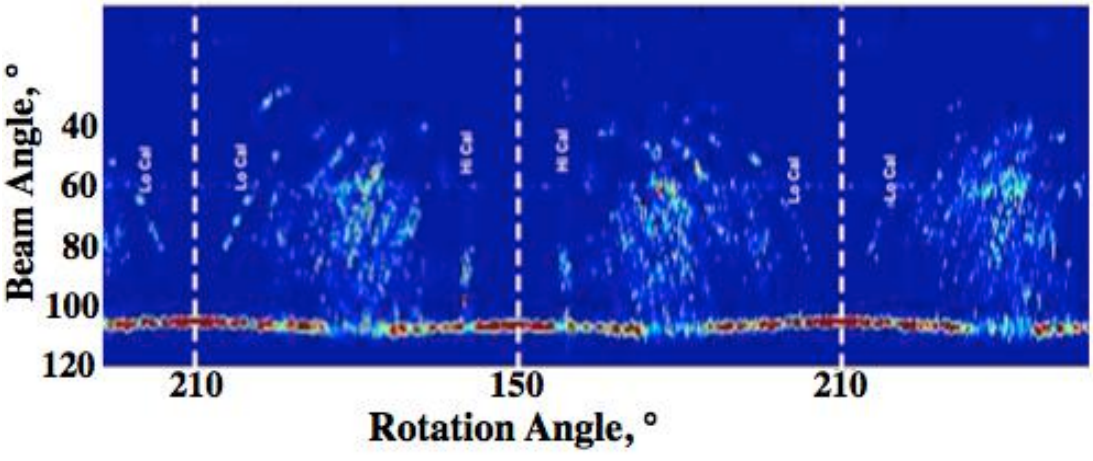

Figure 5. Spherical (time) slices showing Shane Seep and two calibration air flows, labeled on figure from a sonar rotator lander deployment in 2008. Sonar was deployed ~8 m southeast from the main seep bubble plume (see Fig. 1b, relative to origin).

The Cryosphere Discuss., doi:10.5194/tc-2016-156, 2016
Manuscript under review for journal The Cryosphere
Published: 7 July 2016

332 **3. Results**

333 3.1. COP Seep Field Precursor Study

334 The importance of bubble-bubble acoustic interaction was demonstrated for calibration plumes during the
335 scoping study sonar experiment,. Example MBES rotator data are shown in Fig. 5 for a little over a
336 rotation cycle, which includes the main seep and both the high and low calibration bubble plumes. Arctic
337 weather challenges limited the rotator lander deployment to just a few hours.

338 Sonar returns for the two calibration plumes (Fig. 5) were thresholded above background (bubble-free
339 water) and integrated for each beam during rotation across each calibration plume. The thresholded sonar
340 return in a depth window then was fit with a linear polynomial of the log of the integrated sonar return
341 over the plume, σ, versus height, *h* (Fig. 6). The value of σ increased as the bubble plume rose – i.e., σ(*h*)
342 was not constant – even though air bubble volume change is minimal over such short rise heights. This is
343 evidence of bubble-bubble acoustic interaction decreasing as the bubbles rise and spread from turbulence
344 (acoustic interactions decrease towards zero as the inter-bubble distances increases to large distances).

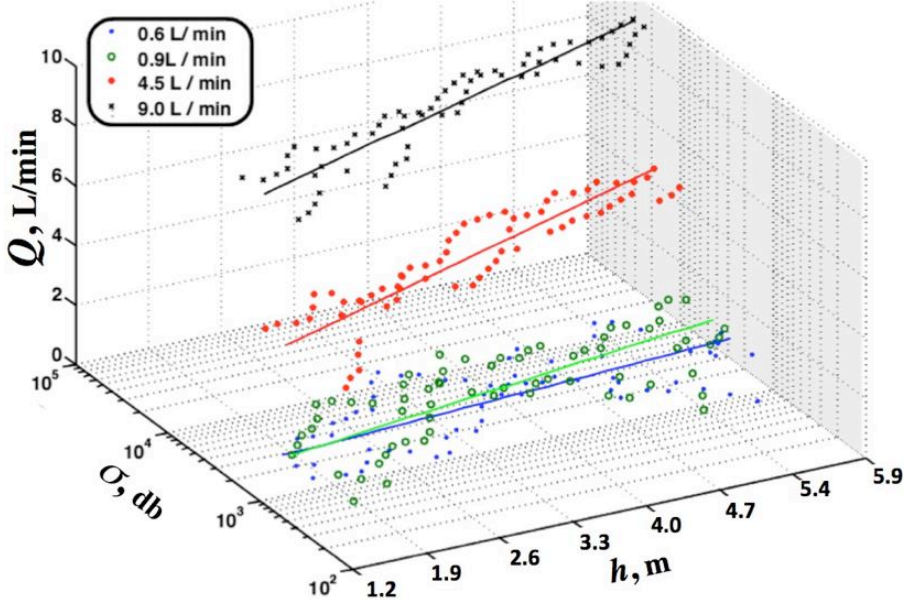

345

346 **Figure 6.** Field sonar calibration return, σ, from the Coal Oil Point seep field for air bubbles in 22-m deep
347 water. Sonar return integrated across the plume, σ, versus airflow, *Q*, and height above seabed, *h*, for four
348 airflows and least-squares linear-regression fits to log(σ) versus *h*.

The Cryosphere Discuss., doi:10.5194/tc-2016-156, 2016
Manuscript under review for journal The Cryosphere
Published: 7 July 2016

3.1. Calibration

In situ calibration experiments were conducted in the Kara Sea (neighboring the Laptev Sea) in a region of no natural seepage and almost flat seafloor to reduce or eliminate off-beam acoustic seabed scattering. Winds were unusually calm for this region, 1-3 m s^{-1}, with no significant waves (0 to 1 ball). Column profile temperature and salinity data were obtained by a conductivity temperature depth, CTD (SBE19+, Seabird, USA). The vessel was anchored during the calibration experiments. The wave-mixed layer (WML) extended to ~35 m depth, with upper water warmer by ~3.5°C than deeper water (Fig. 7A).

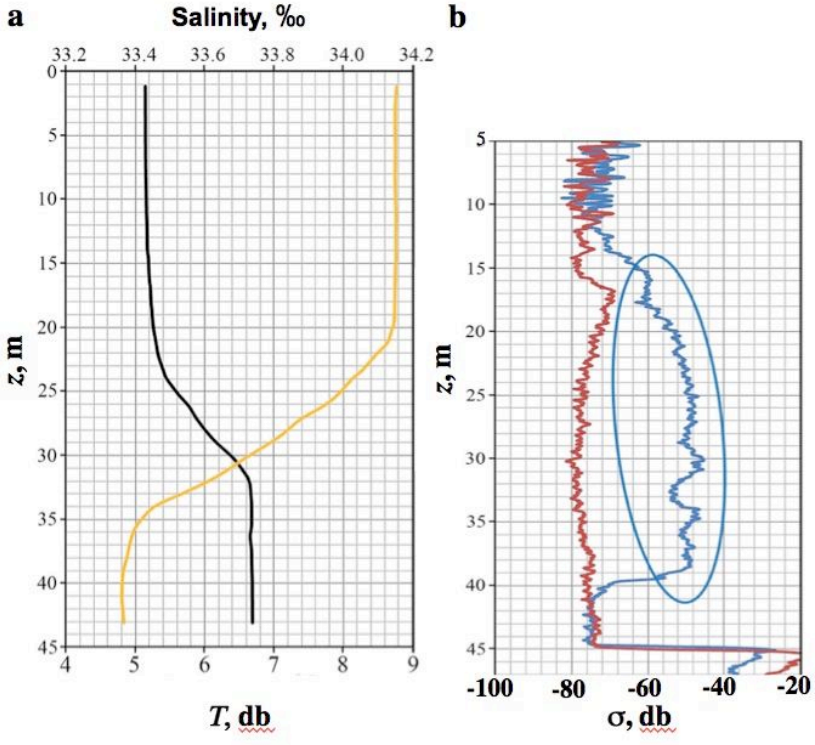

Figure 7. a. Salinity, and temperature, *T*, depth, *z*, profile during bubble plume calibration experiment in the Laptev Sea. **b.** Single beam echosounder sonar return integrated across the plume, σ, with *z* for no bubble plume (red) and a bubble plume (blue), bubble plume σ circled.

Bubbles have high density-contrast with water and thus are strong sonar targets that are distinguished easily from the background (Fig. 7b). SBES data contains significant geometric uncertainty, which is evident in the overlap in time of sonar returns for the calibration bubble plume (Fig. 8) and results from current advection of the plume orthogonal to the page. MBES addresses this SBES deficiency. For

The Cryosphere Discuss., doi:10.5194/tc-2016-156, 2016
Manuscript under review for journal The Cryosphere
Published: 7 July 2016

example, the SBES sonar loses the bubble plumes once they have entered the wave mixed layer, where currents often shift, but the multi-beam sonar continues to follow them to 13 m depth, slightly below the draft of the R/V *Viktor Buynitsky*.

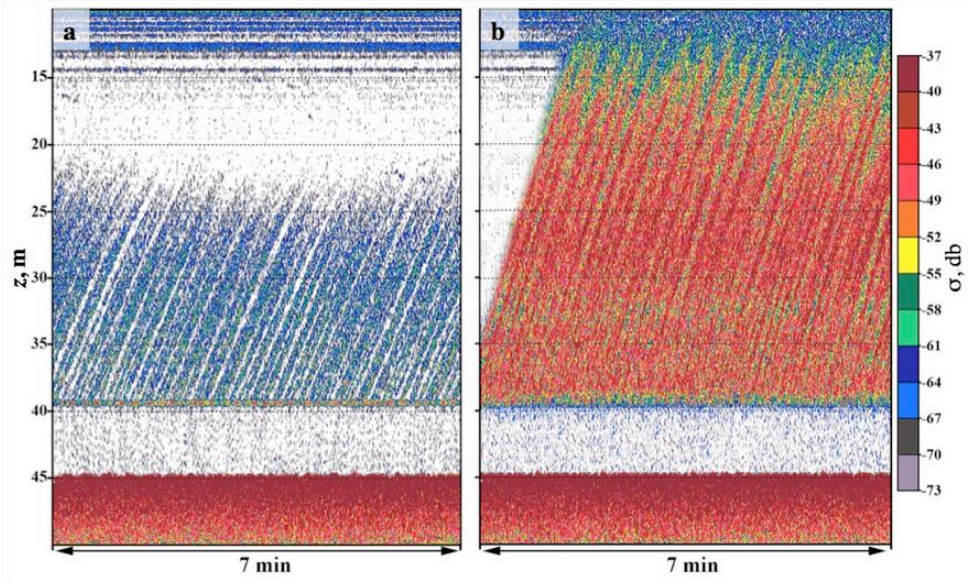

Figure 8. Plume-integrated sonar return, slume-icalibration bubble plume from 40-m depth, *z*, experiment conducted for **a.** 0.042 L/min and **b.** 1.1 L/min at 5.5 bar for the single beam sonar.

Data analysis and visualization was performed with custom MatLab routines (Mathworks, Mass.) that first geo-rectified each ping and then assembled the data for each experimental run into a 3-dimensional array of depth, *z*, transverse distance, *x*, and along track distance, *y* (or time, *t*, if stationary).

Noise is the most common sonar return and was isolated from the bubble-plume signal based on setting a threshold from the sonar return occurrence distribution, $\Psi(\sigma)$ (Fig. 9a). $\Psi(\sigma)$ showed a noise $\Psi(\sigma)$ at approximately -80 db that clearly is distinct from the stronger, but less common, bubble $\Psi(\sigma)$ seen in Fig. 7b, for example. Based on inspection of $\Psi(\sigma)$, a noise threshold value of -70 db was selected, which provided a 5-8 db transition between noise and bubbles (Fig. 9a, arrow). In addition, obvious sonar artifacts, which can exhibit strong sonar return signatures, were masked by a swath constraint–i.e., spatial segregation. Specifically, the plume center was identified at each depth-filtered to ensure continuity with depth and only samples within a specified horizontal distance from the plume centerline that tightly constrained the plume above the noise threshold were incorporated into the analysis.

The Cryosphere Discuss., doi:10.5194/tc-2016-156, 2016
Manuscript under review for journal The Cryosphere
Published: 7 July 2016

For the calibration experiments, plumes with volume flux, Q, from 0.019 to 1.1 L/s were created and observed by both SBES and MBES systems (Fig. 9). The contribution of bubble plume weak and strong sonar returns were investigated by their signature in $\Psi(\sigma)$. Specifically, $\Psi(\sigma)$ was modeled by a piece-wise least-squares, linear-regression analysis of $\Psi(\sigma) = a\sigma(z)^b$, which then was compared to expected trends in plume evolution of a rising bubble plume. Fit parameters are shown in Supplemental Table S1, with example data and fits for the 0.8 L/s plume shown in Figs. 9d-9f for three depth windows (all below the WWML).

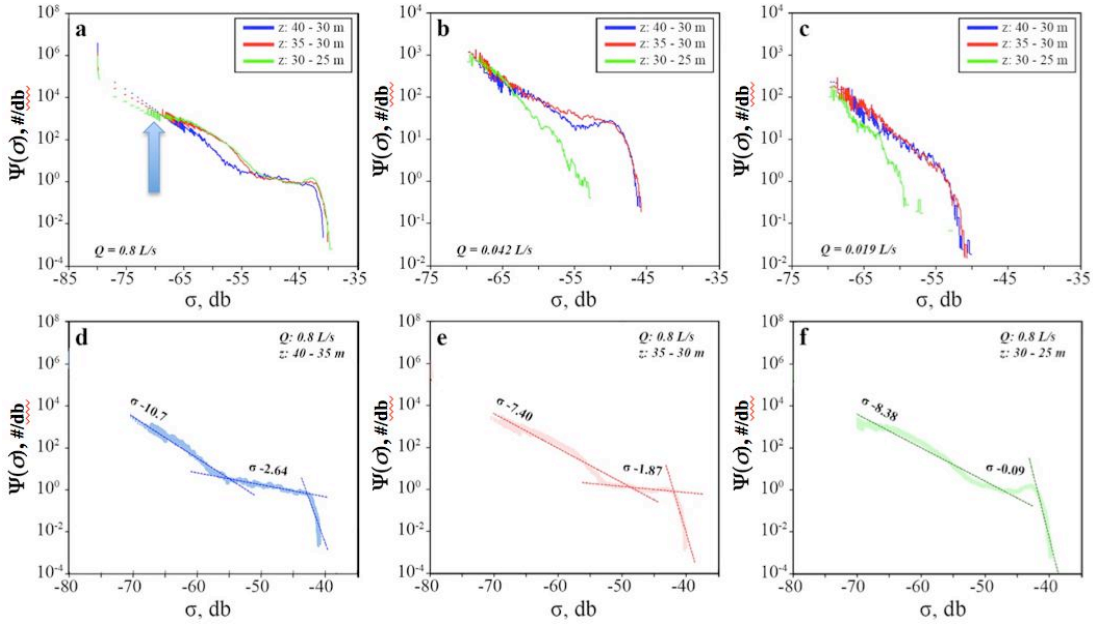

Figure 9. Plume-integrated sonar return, σ, occurrence, Ψ, normalized to sonar bin-width (sonar bins are logarithmically spaced) for **a.** full water-column for a flow, Q, of 0.8 L/s – unthrestholded for processed depth windows, z, arrow shows noise threshold. $\Psi(\sigma)$ thresholded for **b.** Q = 0.042 L/s, **c.** 0.019 L/s and with linear fits for Q = 0.8 L/s for **d.** z = 35-40 m, **e.** 30-35 m, **f.** 25-30 m. Data key on figure. Fit parameters in Supplemental Table S1.

$\Psi(\sigma)$ for low and high flows exhibited distinctly different characteristics with $\Psi(\sigma)$ for the intermediate-flow plume exhibiting characteristics of both low and high flows. A weak sonar return represents small bubbles, while strong returns may reflect large bubbles or it may reflect dense aggregations of small and/or large bubbles. Thus, as a bubble plume rises, the relative importance of small bubbles should increase as small bubbles disperse from the plume, spreading the weak sonar return over a larger volume. The weakest flow plume shows a clear trend of a two-part power law at the deepest depth for $\Psi(\sigma)$ (Fig.

The Cryosphere Discuss., doi:10.5194/tc-2016-156, 2016
Manuscript under review for journal The Cryosphere
Published: 7 July 2016

401 9c; Supplemental Table S1); however, Ψ(σ) remained constant for both weak and strong returns as the
402 bubble plume rose (steepening increases the relative importance of weaker σ) to 30 m then steepening
403 abruptly, emphasizing smaller bubbles (*b* = -8, -7, -12 for weak σ for the 45-40, 40-35, 35-30 m depth
404 windows, respectively). For the weaker flows, 0.042 and 0.019 L/s (Figs. 9b, 9c), the strongest sonar
405 returns disappear completely at the shallowest depth, consistent with bubble-plume dispersion and bubble
406 dissolution.

407 The deepest depth window for the high-flow plume (Fig. 9d) exhibits a bi-modal Ψ(σ) with stronger
408 returns more common relative to weaker returns than in the low flow plume (Fig. 9c) or than "predicted"
409 by extrapolating the power law ($\sigma^{-10.7}$) to the stronger returns (Figs. 9d and 9f, respectively). As this
410 plume rose, Ψ(σ) for the weak σ decreased in relative importance while Ψ(σ) for stronger σ remains
411 constant – the power law exponent, *b*, for the intermediate depth (-7.4) was less steep than for the deeper
412 (-10.7) and shallower (-8.4) depths. Thus, most of the evolution of Ψ(σ) is due to a spatial expansion of
413 weaker σ (i.e., smaller bubbles), while the strong σ bubbles remain relatively uniformly constrained with
414 depth. The overall increase in σ with rise is the same character observed in the precursor study (Fig. 6),
415 which featured strong flows comparable to those shown in Figs. 9d-9f.

416 Ψ(σ) for the intermediate flow plume (Fig. 9b) shares characteristics of both the high and low flow plume
417 Ψ(σ), bi-modal at the deepest depth with a pronounced strong σ peak in Ψ(σ) (like the high flow plume)
418 evolving into a dual power law as the plume rises (like the low flow plume Ψ(σ). Thus, Ψ(σ) for the
419 intermediate flow plume evolved through the patterns of the strong and weak flow plumes as it rose.

420 These plumes all originate from a point source and disperse as they rise, thus bubble-bubble acoustical
421 interactions should decrease as the bubbles rise. With the exception of the strongest plume, plume rise
422 decreases σ; however, for the strongest flow plume, rise initially increases return, similar to the trend in
423 the precursor study (Fig. 6), which was for comparably high flows, albeit over fewer depths much closer
424 to the source. Example MBES data are presented in the Supplemental Materials, Figs. S1 and S2.

425 The depth and flow dependent sonar calibration curves, σ(*Q*,*z*), were derived to account for the depth-
426 evolution of bubble-bubble acoustic interactions as the bubbles rise (Fig. 10). Specifically, σ above the
427 noise threshold in the spatially-segregated boxes in each depth window was averaged across 7-minutes of
428 sonar data to derive σ(*Q*,*z*). The MBES and SBES calibration datasets show saturation at high flow,
429 similar to Greinert and Nützel (2004), which is evidence of bubble-bubble acoustical interaction. For high
430 flows, this likely includes sonar shadowing of more distant bubbles by nearer bubbles (decreasing total
431 return). At low flow, sonar return increases with increasing flow at a rate far faster than linear addition of

The Cryosphere Discuss., doi:10.5194/tc-2016-156, 2016
Manuscript under review for journal The Cryosphere
Published: 7 July 2016

the number of bubbles–for a flow doubling (Q=0.02 to 0.04 L/min), σ should only increase ~6 db ($20\log_{10}(2)$), yet increases are much larger.

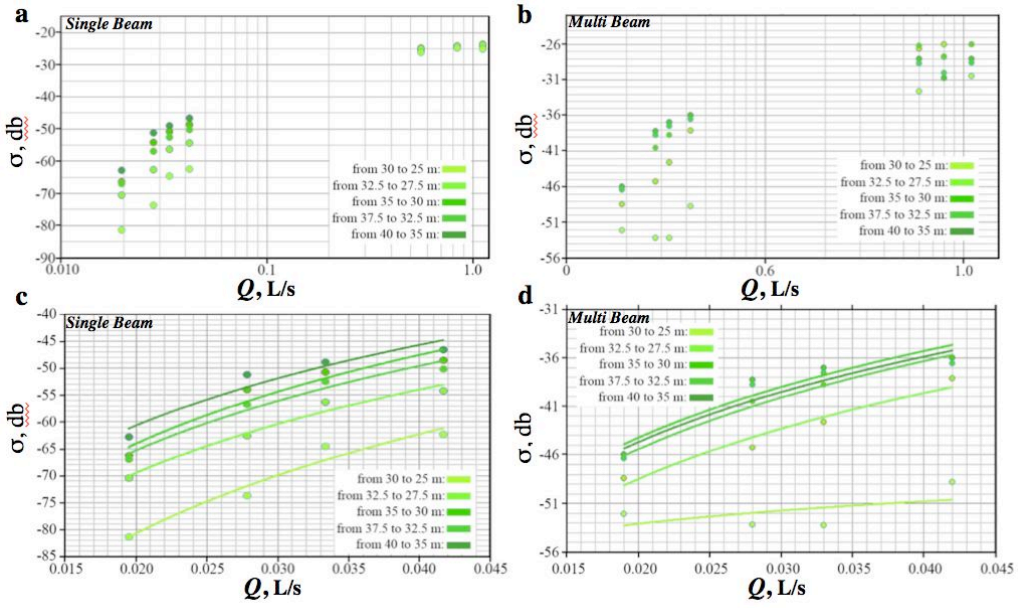

Figure 10. Sonar return, σ, with respect to volumetric flux, Q, calibration curves for the single-beam sonar for **a)** all Q, and **c)** low Q, and for the multibeam sonar for **b)** all Q and **d)** low Q. Fit parameters are shown in Supplemental Table S2.

The calibration curves confirmed the existence of a depth dependency in σ for both SBES and MBES systems (Fig. 10). For low flow plumes, σ decreases with rise and is non-linear with Q. In contrast, for high flows, both SBES and MBES saturate or are near saturation although there is significantly more variability in the MBES data. Close inspection of the high-flow plume MBES data revealed undulations, which may have led to depth aliasing of the return in the 5-m depth windows. The high flow calibration plumes are relevant for major seep bubble plumes such as in COP seep field; however, plumes in the ESAS study area were not this strong, and the strong calibration plumes are not discussed further. In contrast, the low flow calibration plumes are comparable to typical minor bubble plumes (Leifer, 2010) and span the range of natural seepage observed in the study area.

These *in situ* calibration curves were derived for application to seep bubble sonar survey data, and accounts for the vertical velocity of the bubbles, which includes the upwelling flow, which is itself dependent on the flux (Leifer, 2010). However, the calibration curve should account for the difference in

The Cryosphere Discuss., doi:10.5194/tc-2016-156, 2016
Manuscript under review for journal The Cryosphere
Published: 7 July 2016

depth between the seep study area and the calibration plumes (70 m versus 40 m) and in composition – the seep gas primarily was methane, while the calibration gas was nitrogen. Both of these factors have non-negligible implications for the bubble dissolution rates of the two different plumes. As a result, the calibration should account for the differing dissolution rates and thus differing mean volume flux over the depth windows.

3.2. Bubble Dissolution Rates and Volume Flux

Bubble dissolution or gas outflow for each gas species, *i*, is driven by the concentration difference, ΔC, between the bubble and the surrounding water,

$$F_i = k_{Bi} A(\Delta C_i) = k_{Bi} A(C_i - H_i P_i) \quad (4)$$

where k_B is the individual bubble gas transfer rate and depends on the gas diffusivity, A is the bubble surface area, H is the Henry's Law equilibrium, and P is the bubble partial pressure. To address the difference in seep and calibration gases, a numerical bubble propagation model was used to explore the relative dissolution rates for the two types of bubble plumes. The bubble model is described elsewhere (Leifer et al., 2006; Leifer et al., 2015; Rehder et al., 2009). In brief, it solves the coupled differential equations describing bubble molar content (Eqn. 4), size, pressure, and rise for each bubble size class in a bubble plume.

Bubble size distributions, **Φ**, for the calibration and seep bubble plumes were not measured, thus, modeling provides a first attempt to quantify the biases that can be introduced. Implications of these simplifying assumptions are discussed in Section 4.4. The model was initialized with a typical (Leifer, 2010) minor **Φ** (Fig. 11a) for either CH_4 or nitrogen bubbles, dissolved air gases at equilibrium in the water column, the observed CTD profile (Fig. 11b), and a 10 cm s^{-1} upwelling flow. This is an average upwelling flow, which is too low for the highest calibration flow and too high for the lowest (Leifer, 2010).

The Cryosphere Discuss., doi:10.5194/tc-2016-156, 2016
Manuscript under review for journal The Cryosphere
Published: 7 July 2016

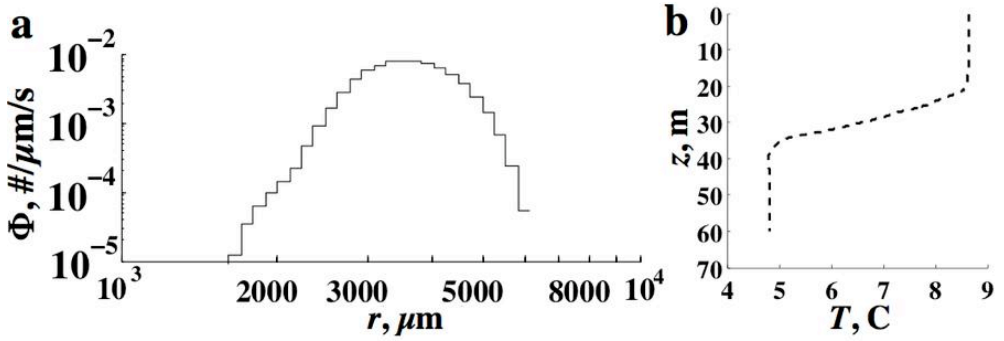

Figure 11. a. Minor bubble plume size distribution, Φ, with respect to radius, *r*, used to initialize the bubble model. **b.** Temperature, *T*, depth, *z*, profile used in model.

As a nitrogen bubble rises, it grows primarily due to decreasing hydrostatic pressure, and to a lesser extent from oxygen inflow, while it shrinks from nitrogen outflow (Fig. 12). The numerical simulations show that for the first three, 5-meter depth windows, the depth-averaged total bubble plume volume, $\langle Q_z \rangle$, increases (Fig. 12b) by 4.7%, 15%, and 29%, respectively.

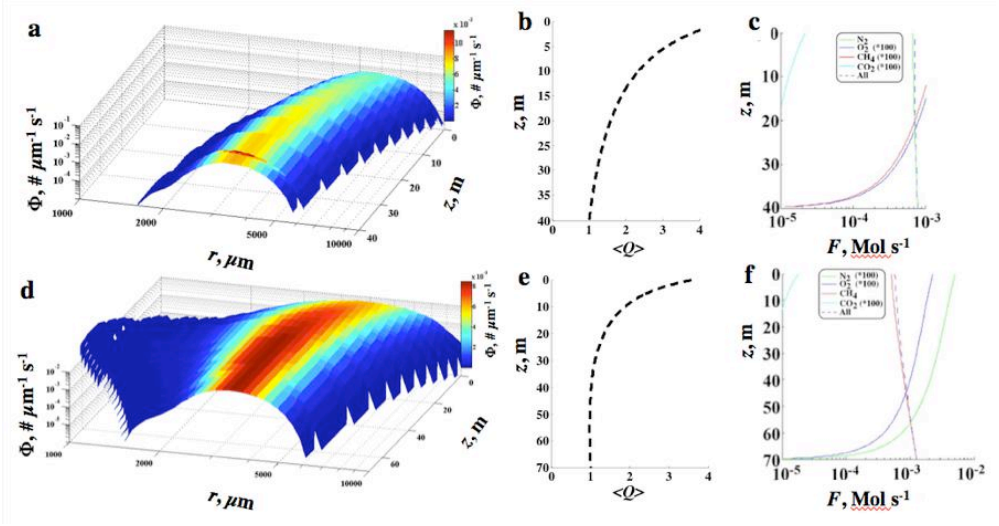

Figure 12. a Depth, *z*, evolution of the bubble plume size distribution, Φ, for a nitrogen minor plume (calibration) from 40 m and **d** for a CH_4 seep plume from 70 m. Seabed normalized volume averaged over depth window, $\langle Q \rangle$, of the rising bubble plume for **b.** calibration plume, and **e.** seep plume. Molar vertical flux for **c.** calibration plume, and **f.** seep Data keys on panels.

In contrast to the 40-m nitrogen calibration bubble plume, there are dramatic changes in the size distribution of a pure CH_4 minor seep bubble plume rising from 70-m depth with the smallest bubbles

The Cryosphere Discuss., doi:10.5194/tc-2016-156, 2016
Manuscript under review for journal The Cryosphere
Published: 7 July 2016

487 dissolving and the largest bubbles growing (Fig. 12d). Overall, air uptake and decreasing hydrostatic
488 pressure largely balance dissolution for the plume overall for the first 50 m of bubble rise and $<Q_z>$
489 remains roughly stable (Fig. 12e) – Q decreases by 0.7%, 0.2%, and 0.0% in the first three 5-meter depth
490 windows, respectively. Note, stable Q does not imply constant total CH_4 bubble content, which
491 continually outflows the rising bubble.

492 The volume correction factors between the calibration-plume and the seep plume are 0.948, 0.868, and
493 0.775 for the 65-70, 60-65, and 55-60 m depth windows, respectively. This shows that the calibration
494 plume Q averaged over the 35-40 m depth window is ~5% greater than the seep bubble plume Q for the
495 70-65 m depth window.

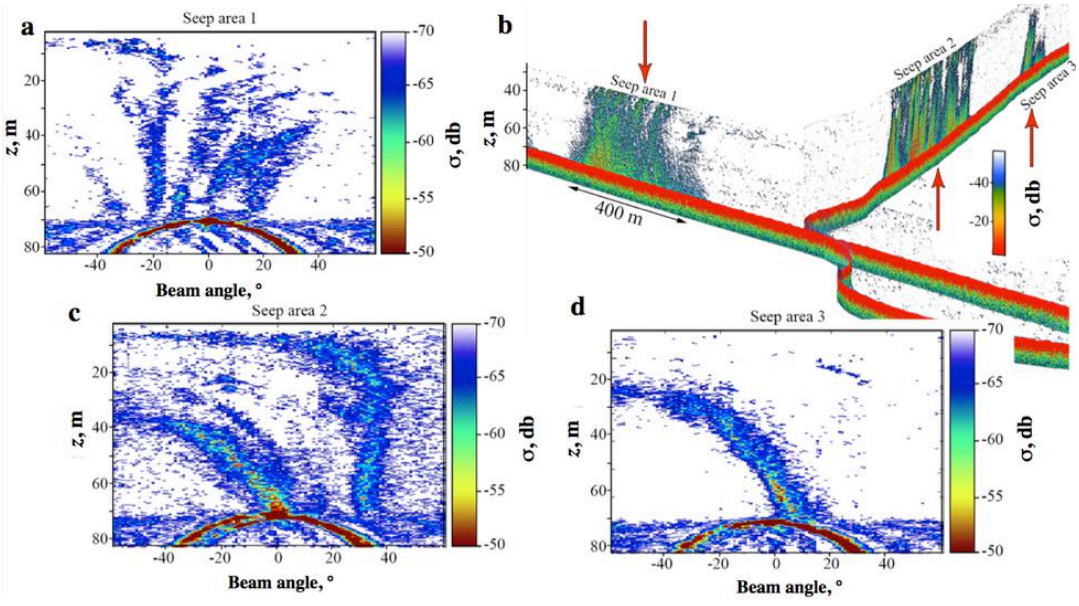

496
497 **Figure 13.** Sonar return, s, with depth, z, of seep bubble plumes in the Laptev Sea. **a. c. d.** Multibeam
498 sonar data, single ping, in each of the seep areas, locations labeled on b. **b.** Single beam sonar data. Size
499 scale and data key on panels.

500 **3.3. Natural Seepage Sonar Observations**

501 The depth-dependent calibration was applied to seep sonar data collected in the Laptev Sea for 70-m deep
502 water under conditions of strong currents (Fig. 13). Three seep areas were surveyed, two weak and one
503 strong, all with numerous plumes. The MBES data illustrates the additional spatial information missing in
504 SBES systems. For example, Seep Area 1 in the SBES data (Fig. 13b) appears to show extensive diffuse
505 seepage, which the MBES data (Fig. 13a) reveals is many low-flow discrete bubble plumes.

The Cryosphere Discuss., doi:10.5194/tc-2016-156, 2016
Manuscript under review for journal The Cryosphere
Published: 7 July 2016

506 The flux for the seep areas (Fig. 14) was mapped by averaging the seepage flux in the 65-70 m depth
507 window in 1-m^2 quadrats after application of the calibration curves and correction factors. The deepest
508 depth window was chosen to preserve better the seabed location of emissions for spatial analysis.

509 Seep Area 2 was stronger than the other seep areas by an order of magnitude and clearly showed a
510 northeast-southwest trend, which also is apparent in all seep areas. Note, some of the striation patterns,
511 primarily of the weaker returns, are consistent with the very strong currents detraining small bubbles out
512 of the plume in the direction of the sonar beam fan. On a second, east-west leg, Seep Area 1 was surveyed
513 with currents not-aligned with the sonar beam fan and does not exhibit the striation. Further evidence of
514 this current effect is shown in the sonar ping data (Fig. 13a vs. Figs. 13c and 13d); where Seep Area 1
515 does not show the extreme tilt across beams as in sonar data for Seep Areas 2 and 3. Thus, the linear seep
516 trends must reflect geological control.

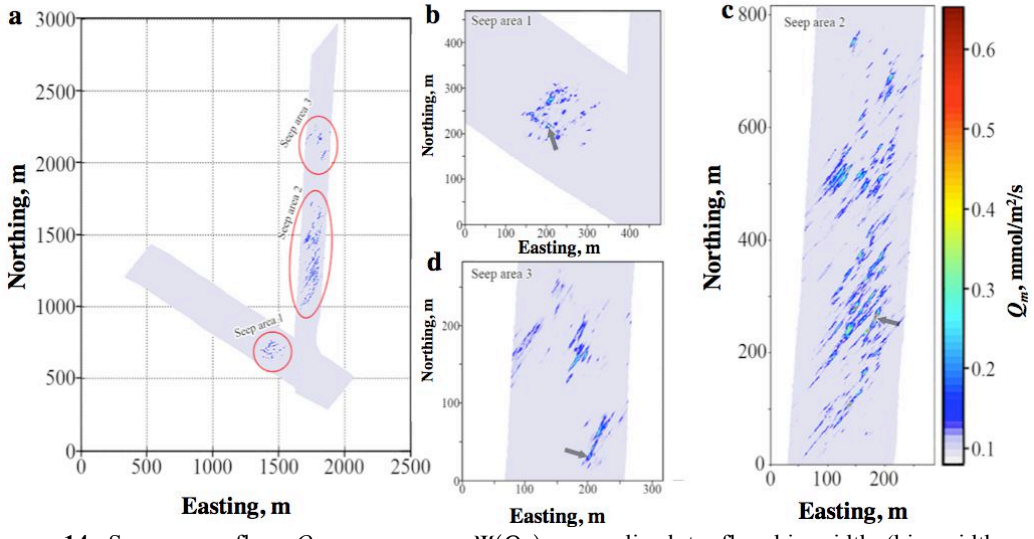

517
518 **Figure 14.** Seep mass flux, Q_m, occurrence, $\Psi(Q_m)$, normalized to flux bin-width (bin widths are
519 logarithmically-spaced) for **a** all seep areas, and for **b-d** Seep Areas 1-3 with power law fits. Data key on
520 panel a. Fits in Table 2.

521 Seepage spatial structure showed numerous seeps clustered around the strongest seep with an apparent
522 modulation at distances of ~100 m (Supp. Fig. S4). In seepage areas 1 and 2 the dominant seep plumes
523 were as strong as 0.3 mmol m^{-2} s^{-1} (7.4 cm^3 s^{-1}) while the dominant seep plumes in the stronger Seep Area
524 2 (Fig. 13c) released >0.6 mmol m^{-2} s^{-1} (15 cm^3 s^{-1}).

The Cryosphere Discuss., doi:10.5194/tc-2016-156, 2016
Manuscript under review for journal The Cryosphere
Published: 7 July 2016

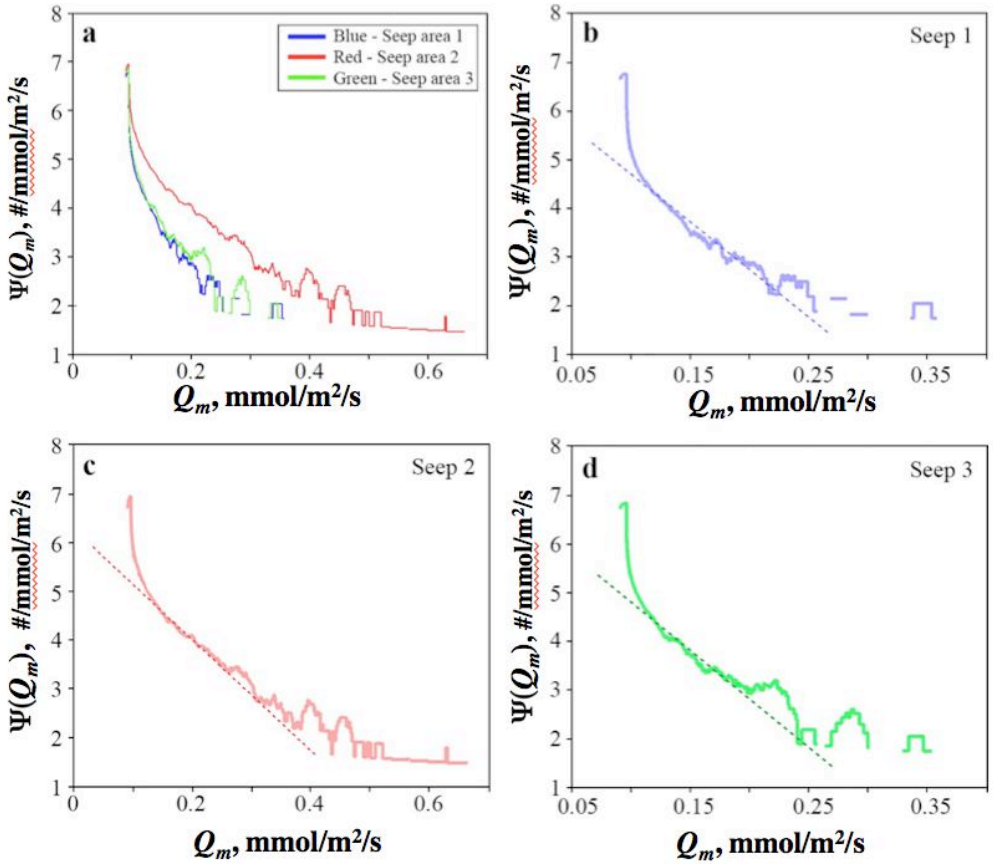

Figure 15. Seep mass flux, Q_m, occurrence, $\Psi(Q_m)$, normalized to flux bin-width (bin widths are logarithmically-spaced) for **a** all seep areas, and for **b-d** Seep Areas 1-3 with power law fits. Data key on panel a. Curve fits presented in Table 2.

The mass flux, Q_m, occurrence distribution, $\Psi(Q_m)$, was calculated for each seep area and showed Seep Area 2 contained the largest number of strong seep plumes followed by Seep Area 3 and then Seep Area 1 (Fig. 15). For these seep areas, $\Psi(Q_m)$ for weak emissions asymptotically approached ~0.1 mmol/m^2/s (2.5 cm^3/s)–the noise level. Thus, the calibration flows (Fig. 10) bracketed from the MBES noise level to the largest observed seep plume. Seep Area 2 exhibits both greater fluxes and a shallower power law (Fig. 15c). Furthermore, all three seep areas exhibited positive anomalies or peaks in $\Psi(Q_m)$ for stronger flux seepage. These peaks signify a preferred emission mode–i.e., multiple seeps with similar emission fluxes.

For weaker seeps with good signal to noise (Q_m > 0.15 mmol/m^2/s), the power law fits are nearly identical, 6.65, 6.27, 6.80 (Table 2) for Seep Areas 1, 2, 3, respectively. Total flux in each seep area was determined

The Cryosphere Discuss., doi:10.5194/tc-2016-156, 2016
Manuscript under review for journal The Cryosphere
Published: 7 July 2016

by area integration and was 5.56, 42.73, and 4.88 mmol/s for the MBES data (Table 2). SBES-derived emissions were biased lower compared to MBES, by 3.7% - 36% for the seep areas, with best agreement for Seep Area 2.

TABLE 2 HERE

4. Discussion

4.1. Bubble-Bubble Acoustic Interaction

We presented results of an *in situ* experiment to investigate the evolution of bubble plume sonar return from rising engineered bubble plumes spanning two orders of volume flow rates from flows that were comparable to typical minor plumes and very strong major plumes at the high end (Leifer, 2010). Calibration plume sonar return increased strongly and non-linearly with flux, ~15 db for a flow doubling from 0.02 to 0.04 L/s. This increase is faster than the 6 db increase that would be expected by simply summing the sonar cross sections of the doubled number of bubbles. Instead, the increase suggests strong bubble-bubble acoustical interactions. Specifically, with increased flow, overall plume dimensions expand more quickly, leading to less bubble shadowing and shallower sonar occurrence slopes at the same height above the nozzle (Fig. 10). In contrast to the overall plume dimensions, which include smaller more dispersed bubbles, the dense core of large bubbles tends not to disperse and is largely insensitive to height (Fig. 9). Thus, for the dense plume core, increased flux increases bubble shadowing such that the signal of the additional bubbles is blocked by other bubbles and sonar return becomes nearly independent of flow, i.e., saturated (Figs. 10a and 10b). Greinert and Nützel (2004) observed similar behavioral regimes for air bubble plumes in far shallower water. Thus, the calibration bubble plume provides strong evidence of non-negligible bubble-bubble acoustical interaction at both low and high flow rates. Furthermore, the non-linearity of the relationship is shown by the relationship between σ and Q as the bubble plume rises and disperses. Thus, bubble-bubble acoustic interactions remain significant even after the plume has risen 15 m.

As high-flow bubble plumes rise, the weak sonar return portion of the plume evolves due to small bubble dispersion, leading to an increase in the integrated sonar return (Fig. 9), a pattern observed for the air calibration experiment in the Coal Oil Point (COP) seep field (Fig. 6). In the COP seep field study, calibration flows extended from comparable to far higher flows than those reported herein, and found that the depth-dependent sonar return increased with height on finer depth scales (Fig. 6) than obtainable in the Arctic experimental configuration. This is interpreted as due to decreased bubble “shadowing” of more distant bubbles as the plume expands. In the case of the ESAS calibration flows, the depth evolution

The Cryosphere Discuss., doi:10.5194/tc-2016-156, 2016
Manuscript under review for journal The Cryosphere
Published: 7 July 2016

of the sonar occurrence distributions showed a strong influence from small bubble dispersion leading to an expansion of the plume volume and an increase in integrated sonar return.

As the low-flow calibration plumes rise and disperse, sonar return decreases. Overlapping intermediate depth windows were evaluated and confirmed this was not an artifact of plume oscillatory motions aliasing the return signal across the depth windows. The decrease in overall sonar return with rise is (by definition) a decrease in scattered sonar energy. This suggests that greater energy scatters back to the sonar when the plume is spatially denser.

4.2 Bubble Detrainment and Bubble-Bubble Acoustic Interaction

The current artifact striations in the natural seep sonar data are consistent with the importance of bubble-bubble acoustic interaction. Specifically, where seep bubble plumes were imaged under high currents, small bubbles were advected out of the plumes into the downcurrent water in the beam fan, and observed, but not when the beam fan was perpendicular to the currents. In the case of the beam-fan-current co-orientation, scattered acoustic energy interacts with nearby downcurrent bubbles, which are in the beam – the cross-track beam is broad (120°), while the along-track beam is narrow. In contrast, when cross-oriented, the sonar beam fan fails to image the detrained bubbles. This provides clear evidence of bubble-bubble acoustic sonar interactions for distances larger than the plume dimensions.

4.3. Weak and Strong Sonar Bubble Contributions

The sonar occurrence distributions were bimodal for intermediate and strong calibration plume. Specifically, weak sonar returns were well described by a steep power law (σ^{-b}, $b > 7$) for high σ, and for all but the weakest plumes, a gently sloped "shelf," which in the intermediate flow case (Q = 0.42 L/s) was negative leading to a second peak. These changes mimic those observed in how the bubble size distribution changes with increasing flow reported in Leifer and Culling (2010). In that study, with increasing flow, the low flow plume bubble distribution is a narrow Gaussian (minor bubble plumes), which shifts to a power law at high flow (major bubble plumes) that spans small to very large bubbles. Intermediate flows exhibit characteristics of both. A steep power law implies spatial constraint–i.e., bubbles are not dispersing and creating returns across a spectrum of strengths. Furthermore, the occurrence of strong return is invariant with depth for the strong plume (Fig. 9a), indicating that the large bubble core of the strong plume remains spatially constrained. At intermediate flows, the sonar occurrence distribution infills–creating a shallow power law for higher flows and stronger returns. In contrast, turbulence and currents tend to disperse small bubbles, which are present in both weak and strong flow bubble plumes. As the plume rises, the signal from these bubbles eventually become lost to

The Cryosphere Discuss., doi:10.5194/tc-2016-156, 2016
Manuscript under review for journal The Cryosphere
Published: 7 July 2016

dissolution and dispersion that reduces sonar return signal to the noise level, leading to a steepening of the sonar return occurrence distribution for weak returns.

4.4. Bubble Size Distribution

Bubble size distributions have been reported for other Arctic seep sites (Shakhova et al., 2015), but equipment to make such measurements were unavailable for this study. Low flow seep plumes are termed minor (Leifer, 2010) and are well described by a Gaussian function (Leifer and Culling, 2010). With increasing flux, the peak radius of the plume increases, until a critical flux above which the bubble size distribution becomes more complex, until eventually being described by a power law, termed major (Leifer and Culling, 2010). The transition from minor to major depends on sediment characteristics and physical oceanographic conditions such as temperature and salinity that affect bubble plume formation (Asher et al., 1997; Haines and Johnson, 1995).

Bubble modeling was used to address the effect of evolving bubble size distribution with flow in application of calibration air or nitrogen (preferred for safety reasons) bubble plumes to seep bubble plumes. In this study, we applied a first approximation using a typical minor bubble plume size distribution. Clearly initializing the model with measured plumes would improve the accuracy of the volume correction factor and hence sonar-derived flux. Still, the primary goal in our study is to demonstrate with a simple approximation that bubble size matters and should not be neglected.

Although the simulations were conducted to correct between a nitrogen calibration plume and pure methane seep bubbles, a compressed air calibration plume could be used and would behave highly similar. If the seep bubbles contain other non-trace gases, their outgassing could impact significantly bubble size evolution with rise. This is particularly relevant for a gas like carbon dioxide, which is far more soluble than methane, and thus can lead to rapid bubble size change in the deepest depth windows. Note, bubble dissolution is strongly depth dependent (Leifer and Patro, 2002a) and thus the greater the depth discrepancy between calibration plume and seep plume, the larger the correction factor.

The sonar return of a bubble depends on its size (and shape which depends on size) and relationship to flux also depends on the vertical rise rate including upwelling flows. Thus, future studies should investigate both the size distribution and upwelling flow for a range of flow rates.

4.5. Field Comparison of MBES with SBES

The MBES and SBES systems were calibrated with the same nitrogen gas bubble plumes, thus the two systems should agree in terms of flux observations. Calibration flows spanned very weak flow (Q = 0.19 L/s) to very strong flows (Q = 1.1 L/s). The low flow calibration bubble plume was below the seep field

The Cryosphere Discuss., doi:10.5194/tc-2016-156, 2016
Manuscript under review for journal The Cryosphere
Published: 7 July 2016

noise floor of the MBES system, while the high flow was more than an order of magnitude greater than field observations.

Field observations showed far better agreement between systems for Seep Area 2 than the other seep areas (Table 2). This most likely relates to the greater relative importance of stronger seeps that are well above the noise level relative to the other seep areas. The calibration flows (Fig. 10) showed that SBES sonar return was weaker for the same flow than the MBES sonar return. Geometric uncertainty likely played a role in the SBES downward flux bias.

4.6. Seepage Spatial Characterization

The seepage spatial and strength distribution in the ESAS (Fig. 14) share similarities with structures in the COP seep field (Fig. 1). Subsurface geologic structures control the seepage spatial-flux distribution by creating the pathways through which seepage migrates to the seabed and ocean - seepage areas must occur where geologic structures allow. In the COP seep field, strong seepage areas are located at intersecting non-compressional faults and fractures (Leifer et al., 2010). Furthermore, these faults and/or fractures themselves are preferred migration pathways that connect subsurface reservoirs to the seabed, with seepage tending to manifest along their trend (Leifer et al., 2010).

In the ESAS seepage map (Fig. 14), two spatial trends were manifest, one northeast-southwest of individual vents and second a north-south elongation in Seep Area 2. Both trends were aligned with the two weaker seepage areas. Furthermore, the northeast-southwest trend is apparent within Seep Area 2. Here, fractures in submerged permafrost could play a similar role to the role of fault intersections in the COP seep field; however, more extensive seep area mapping is needed for validation, and/or penetrating sonar data that can image near surface rock strata. On smaller length scales, there is an evident striation pattern that defines vent locations suggesting a subsurface linear geological control on meter length scales.

High flow seepage requires high permeability migration pathways, while low flow seepage occurs along low permeability migration pathways if the driving pressure between the deeper reservoir and the seabed is constant across the active seepage area (Leifer and Boles, 2005). Thus, the stronger and more numerous and extensive seepage emissions from Seep Area 2 indicates higher subsurface permeability and subsurface connectivity with more numerous migration pathways than the other seep areas (Fig. 14). Seepage connectivity can be envisioned topologically as an inverted branched structure (Leifer et al., 2004) where central stronger seepage is surrounded (generally) by weaker seepage (Supp. Fig. S4). Given that permeability is inversely related to resistance in the migration pathways, stronger seepage is fed by migration along pathway(s) with lower resistance (higher permeability), while weaker seepage is fed by

The Cryosphere Discuss., doi:10.5194/tc-2016-156, 2016
Manuscript under review for journal The Cryosphere
Published: 7 July 2016

663 migration along pathways with stronger resistance (lower permeability). One implication of a range of
664 migration pathways with different resistance is that lower resistance seepage adjusts to changes in
665 seepage easier than higher resistance seepage – thus strong seeps become stronger, while weak seeps are
666 more likely to activate/deactivate with changes in emissions (Boles et al., 2001; Bradley et al., 2010). The
667 balance between seepage emissions for different migration pathways with a range of permeability
668 underlies the flux occurrence distribution (Fig. 15).

669 The mapped seepage emissions demonstrated highly similar geologic spatio-flux control. Specifically,
670 weak seepage flux exhibited a fractal dimension, *b*, of -6 (Fig. 15), which characterizes how seepage
671 distributes itself between high and low permeability migration pathways. Note, the actual power law
672 likely is slightly exaggerated due to bubble detrainment into the beam fan in Seep Areas 2 and 3, which
673 spreads sonar return spatially; however, Seep Area 1 does not have this beam fan effect, yet exhibited a
674 similar *b* to the other areas. This argues that the shallow seabed structure (fracture, porosity, etc.) related
675 to low permeability migration pathways is common across the areas, with the main controlling factor
676 being the number of bubbles escaping per second per unit area of seabed.

677 This power law does not extend to the largest seep fluxes, which manifest as perturbations (peaks) above
678 b = -6 power law in the flux occurrence plot. Higher flow plumes, and thus high permeability pathways,
679 could represent a failure of the normal seabed structure (that governs the weak seepage) from stresses
680 and/or talik melting, leading to focused high flow migration pathways that help define where the seep
681 areas lie.

682 In the Arctic, subsea permafrost degradation from heating both below (geologic – most strong in faulted
683 zones) and above (riverine inputs and overall Arctic Ocean warming) creates migration pathways that
684 manifest as seep spatio-flux distributions. The presence of active seepage in this region likely relates to
685 these heat flows, with the hotspots likely related to taliks and/or subsea thaw lakes, whose locations are
686 controlled by linear geologic structures. In the ESAS, grabens are often linear structures, which often are
687 correlated with paleo-river valleys, and could also cause small-scale co-aligned fractures that lead to
688 seepage being along linear trends. The similarity in the emission probability distribution power law (b=-6)
689 indicates that subsurface permeability exhibits a fractal distribution that is similar between the three areas
690 – arguing for similar formation mechanism, i.e., taliks. In this case, at the intersection of the two linear
691 trends, where migration is higher and thus heat flow likely is higher, talik evolution would be greater,
692 leading to more higher permeability migration pathways.

693

The Cryosphere Discuss., doi:10.5194/tc-2016-156, 2016
Manuscript under review for journal The Cryosphere
Published: 7 July 2016

4.7. Broader Implications

There are enormous carbon stores sequestered in marine-permafrost in the Arctic, which are of particular concern for release as the warming Arctic Oceans transfer heat faster than from the atmosphere to terrestrial permafrost. Migration from this submerged permafrost reservoir to the ocean has created a vast marine seep field that lies entirely in shallow waters with emissions contributing directly to atmospheric budget (Shakhova et al., 2014). Widespread ESAS seabed bubble emissions have been documented (Shakhova et al., 2014, 2015), demonstrating failure of the permafrost's integrity and making methane and additional organic carbon available for microbial methane generation.

The observations support the hypothesis that the current state of sub-sea permafrost is a controlling factor to the spatial variability in methane seabed fluxes, and is undergoing destabilization from warming (Shakhova et al., 2010a, 2010b). The current state of subsea permafrost beneath the ESAS is a potential key to understanding whether and how, methane preserved in seabed reservoirs, escapes to atmosphere (Shakhova et al., 2009a, b, c; Shakhova et al., 2010a, b). Currently our state of knowledge engenders enormous uncertainty in future emissions in large part due to the paucity of data (Shakhova et al., 2014, 2015). Among the new tools and techniques needed to evaluate these fluxes quantitatively over wide areas, *in situ* calibrated sonar shows significant promise.

4.8. Future Directions

In this study, bubble plume spanning almost two orders of magnitude, from 0.019 to 1.1 L/s were engineered; however, a key intermediate range (0.045-0.8 L/s) was missed. This is the regime where bubble plumes shifts from a non-linear relationship between sonar return and flow to saturation where sonar return is largely independent of flow. Furthermore, experiments should follow the plume for more than 15 m; however, currents made this infeasible. Also, the calibration plumes looked at isolated bubble plumes; however, seep bubble plumes often escape from nearby vents into plumes that eventually merge. Given the importance of bubble-bubble acoustic interactions, calibration studies should compare the same total flux from one to several closely located bubble sources to investigate whether there is convergence between single bubble plumes and multiple bubble plumes with rise height as the plume merge. Finally, studies in calmer waters could elucidate better the importance of small bubbles versus large bubbles to overall sonar return.

This study featured the novel use of a numerical bubble plume model to correct for different size evolution between calibration gas bubble plumes and seep bubble plumes. Uncertainty arises from the bubble size distribution, which needs to be measured for the calibration and seep bubble plumes at

The Cryosphere Discuss., doi:10.5194/tc-2016-156, 2016
Manuscript under review for journal The Cryosphere
Published: 7 July 2016

multiple flow rates. Our approach was a simplified first effort with room for improvement, including measurement of bubble size distributions in the field.

5. Conclusions

In this study, using the calibrated multi-beam and single-beam sonars we improved our ability to map and quantify the methane release from seepage in the Laptev Sea outer shelf where subsea permafrost is predicted to be mostly degraded. We created engineered bubble plumes in situ from 40-m depth spanning almost two orders of magnitude, from 0.019 to 1.1 L/s. Non-linear curves relating sonar return to flux for a range of depths demonstrated significant bubble-bubble acoustic interactions – precluding the use of a theoretical approach of scaling bubble sonar cross section by the size distribution. Analysis of the depth evolution of the bubble plume sonar occurrence for different fluxes found weak sonar return was well described by a power law that likely correlated with small bubble dispersion, while strong sonar returns were largely independent of depth, consistent with a central core of focused large bubbles. As a result, plume sonar occurrence was bimodal for all but the weakest seepage.

The *in situ* calibration curve was applied to a natural seepage area from 70-m depth after accounting for the different volume evolution of the nitrogen calibration plume and the methane seep bubble plume through use of a numerical bubble plume model initialized with a typical (assumed) minor bubble plume size distribution. The bubble model suggests ~5% difference between the calibration and seep plumes over the first 5-m depth window. Three nearby seepage areas with total emissions of 5.56, 42.73, and 4.88 mmol/s from multibeam sonar data were mapped, with good to reasonable agreement (4-37%) between single and multibeam sonar, although single beam emissions were biased lower. Seepage occurrence was bimodal, with weak seepage occurrence in each seep area well described by a power law. This was interpreted as suggesting primarily small minor bubble plumes, while a few stronger seepage plumes were mapped that could be major plumes. Seepage mapped spatial patterns suggested subsurface geologic control along linear trends.

6. Acknowledgements

We thank the crew and personnel of the expedition onboard research vessel *Victor Buinitsky*. We would like to acknowledge financial support from the Government of the Russian Federation (grant #14, Z50.31.0012/03.19.2014), the Far Eastern Branch of the Russian Academy of Sciences (RAS). At different stages work was supported by the US National Science Foundation (OPP ARC -1023281), the US National Oceanic and Atmospheric Administration (Siberian Shelf Study), Russian Foundation for Basic Research (grants #13-05-12028 and 13-05-12041), and Headquarters of the Russian Academy of

Sciences (Arctic Program led by A.I. Khanchuk). N. S. and D. C. acknowledge the Russian Scientific Foundation (grant #15-17-20032).

References

Archer, D. and Buffett, B.: Time-dependent response of the global ocean clathrate reservoir to climatic and anthropogenic forcing, Geochem. Geophys. Geosys., 6, Q03002,, 2005.

Asaeda, T. and Imberger, J.: Structure of bubble plumes in linearly stratified environments, J. Fluid Mech., 249, 35-57, 1993.

Asher, W. E., Karle, L. M., and Higgins, B. J.: On the difference between bubble-mediated air–water transfer in freshwater and sea water, J. Mar. Res., 55, 813-845, 1997.

Bauch, H. A., Mueller-Lupp, T. , Taldenkova, E., Spielhagen, R. F., Kassens, H., Grootes, P. M., Thiede, J., Heinemeier, J., and Petryashov, V. V.: Chronology of the Holocene transgression at the North Siberian margin, Global Planet. Change, 31, 125–139, 2001.

Biastoch, A., Treude, T., Rupke, L. H., Riebesell, U., Roth, C., Burwicz, E. B., Park, W., Latif, M., Boning, C. W., Madec, G., and Wallman, K.: Rising Arctic Ocean temperatures cause gas hydrate destabilization and ocean acidification, Geophys. Res. Lett., 38, L08602, 2011.

Boles, J. R., Clark, J. F., Leifer, I., and Washburn, L.: Temporal variation in natural methane seep rate due to tides, Coal Oil Point area, California, J. Geophys. Res. - Oceans, 106, 27077-27086, 2001.

Bradley, E. S., Leifer, I., and Roberts, D. A.: Long-term monitoring of a marine geologic hydrocarbon source by a coastal air pollution station in Southern California, Atmos. Envir., 44, 4973-4981, 2010.

Clark, J. F., Schwager, K., and Washburn, L.: Variability of gas composition and flux intensity in natural marine hydrocarbon seeps. New Energy Development and Technology (EDT) Working Paper 008, UCEI, 15 pp., 2005.

Clark, J. F., Washburn, L., Hornafius, J. S., and Luyendyk, B. P.: Natural marine hydrocarbon seep source of dissolved methane to California coastal waters, J. Geophys. Res. - Oceans, 105, 11,509-511,522, 2000.

Clift, R., Grace, J. R., and Weber, M. E.: Bubbles, Drops, and Particles, Academic Press, New York, 1978.

Dickens, G. R.: Rethinking the global carbon cycle with a large, dynamic and microbially mediated gas hydrate capacitor, Earth Plan. Sci. Lett., 213, 169-183, 2003.

Drachev, S. S., Kaul, N., and Beliaev, V. N.: Eurasia spreading basin to Laptev Shelf transition: structural pattern and heat flow, Geophys. J. Intnl., 152, 688-698, 2003.

Friedlingstein, P., Cox, P., Betts, R., Bopp, L., von Bloh, W., Brovkin, V., Cadule, P., Doney, S., Eby, M., Fung, I., Bala, G., John, J., Jones, C., Joos, F., Kato, T., Kawamiya, M., Knorr, W., Lindsay, K., Matthews, H. D., Raddatz, T., Rayner, P., Reick, C., Roeckner, E., Schnitzler, K. G., Schnur, R., Strassmann, K., Weaver, A. J., Yoshikawa, C., and Zeng, N.: Climate–carbon cycle feedback analysis: Results from the C4MIP model intercomparison, J. Climate, 19, 3337-3353, 2006.

Gautier, D. L., Bird, K. J., Charpentier, R. R., Grantz, A., Houseknecht, D. W., Klett, T. R., Moore, T. E., Pitman, J. K., Schenk, C. J., and Schuenemeyer, J. H.: Assessment of undiscovered oil and gas in the Arctic, Science, 324, 1175-1179, 2009.

Gramberg, I. S., Kulakov, Y. N., Pogrebitsky, Y. E., and Sorokov, D. S.: Arctic oil and gas super basin, X World Petroleum Congress, London, 93-99, 1983.

Graversen, R. G., Mauritsen, T., Tjernstrom, M., Kallen, E., and Svensson, G.: Vertical structure of recent Arctic warming, Nature, 451, 53-56, 2008.

Greinert, J., McGinnis, D. F., Naudts, L., Linke, P., and De Batist, M.: Atmospheric methane flux from bubbling seeps: Spatially extrapolated quantification from a Black Sea shelf area, J. Geophys. Res., 115, 2010.

Greinert, J. and Nützel, B.: Hydroacoustic experiments to establish a method for the determination of methane bubble fluxes at cold seeps, Geo-Mar. Lett., 24, 75-85, 2004.

804 Haines, M. A. and Johnson, B. D.: Injected bubble populations in seawater and fresh water measured by a
805 photographic method, J. Geophys. Res., 100, 7057–7068, 1995.
806 Holemann, J., Kirillov, S., Klagge, T., Novikhin, A., Kassens, H. and Timokhov, L.: Near-bottom water
807 warming in the Laptev sea in response to atmospheric sea-ice conditions in 2007, Polar Res., 30
808 6425–40, 2011.
809 Hornafius, S. J., Quigley, D. C., and Luyendyk, B. P.: The world's most spectacular marine hydrocarbons
810 seeps (Coal Oil Point, Santa Barbara Channel, California): Quantification of emissions, J. Geophys.
811 Res. - Oceans, 104, 20703-20711, 1999.
812 IPCC: Climate Change 2007: The Physical Science Basis, Contribution of Working Group I to the Fourth
813 Assessment Report of the Intergovernmental Panel on Climate Change, 2007.
814 Judd, A. G. and Hovland, M.: Seabed fluid flow: Impact of geology, biology and the marine environment,
815 Cambridge University Press, 2009.
816 Kirschke, S., Bousquet, P., Ciais, P., Saunois, M., Canadell, J. G., Dlugokencky, E. J., Bergamaschi, P.,
817 Bergmann, D., Blake, D. R., and Bruhwiler, L.: Three decades of global methane sources and sinks,
818 Nature Geosc., 6, 813-823, 2013.
819 Leifer, I.: Characteristics and scaling of bubble plumes from marine hydrocarbon seepage in the Coal Oil
820 Point seep field, J. Geophys. Res., 115, C11014, 2010.
821 Leifer, I.: Seabed bubble flux estimation by calibrated video survey for a large blowout seep in the North
822 Sea, J. Mar. Petr. Geol., 2015. This issue, 2015.
823 Leifer, I. and Boles, J.: Turbine tent measurements of marine hydrocarbon seeps on subhourly timescales,
824 J. Geophys. Res. - Oceans, 110, 2005.
825 Leifer, I., Boles, J. R., Luyendyk, B. P., and Clark, J. F.: Transient discharges from marine hydrocarbon
826 seeps: Spatial and temporal variability, Environ. Geol., 46, 1038-1052, 2004.
827 Leifer, I. and Culling, D.: Formation of seep bubble plumes in the Coal Oil Point seep field, Geo-Mar.
828 Lett., 30, 339-353, 2010.
829 Leifer, I., Jeuthe, H., Gjøsund, S. H., and Johansen, V.: Engineered and natural marine seep, bubble-
830 driven buoyancy flows, J. Phys. Oceanog., 39, 3071-3090, 2009.
831 Leifer, I., Kamerling, M., Luyendyk, B. P., and Wilson, D.: Geologic control of natural marine
832 hydrocarbon seep emissions, Coal Oil Point seep field, California, Geo-Mar. Lett., 30, 331-338, 2010.
833 Leifer, I., Luyendyk, B. P., Boles, J., and Clark, J. F.: Natural marine seepage blowout: Contribution to
834 atmospheric methane, Global Biogeochem. Cycles, 20, 2006.
835 Leifer, I. and Patro, R.: The bubble mechanism for methane transport from the shallow sea bed to the
836 surface: A review and sensitivity study, Cont. Shelf Res., 22, 2409-2428, 2002a.
837 Leifer, I. and Patro, R. K.: The bubble mechanism for methane transport from the shallow sea bed to the
838 surface: A review and sensitivity study, Cont. Shelf Res., 22, 2409-2428, 2002b.
839 Leifer, I., Solomon, E., Schneider v. Deimling, J., Coffin, R., Rehder, G., and Linke, P.: The fate of
840 bubbles in a large, intense bubble plume for stratified and unstratified water: Numerical simulations
841 of 22/4b expedition field data, J. Mar. Petr. Geol., 68B, 806-823, 2015.
842 Leifer, I. and Tang, D. J.: The acoustic signature of marine seep bubbles, J. Acoust. Soc. Am., 121, EL35-
843 EL40, 2007.
844 Lemke, P., Ren, J., Alley, R. B., Allison, I., Carrasco, J., Flato, G., Fujii, Y., Kaser, G., Mote, P., Thomas,
845 R. H., and Zhang, T.: Observations: Changes in Snow, Ice and Frozen Ground. In: Climate change
846 2007 : The physical science basis, Contribution of Working Group 1 to the Fourth Assessment Report
847 of the Intergovernmental Panel on Climate Change, Solomon, S., Qin, D., Manning, M., Chen, Z.,
848 Marquis, M., Averyt, K. B., Tignor, M., and Miller, H. L. (Eds.), Cambridge University Press,
849 Cambridge, UK, 2007.
850 MacDonald, I.: Remote sensing and sea-truth measurements of methane flux to the atmosphere
851 (HYFLUX project), US Department of Energy, National Energy Technology Laboratory, 164 pp.,
852 2011.
853 Makogon, Y. F., Holditch, S. A., and Makogon, T. Y.: Natural gas hydrates - A potential energy source
854 for the 21st Century, J. Petr. Sci. Eng., 56, 14-31, 2007.

855 Minnaert, M.: On musical air bubbles and the sound of running water, Phil. Mag., 16, 235-248, 1933.
856 Nicolsky D., and N. Shakhova: Modeling sub-sea permafrost in the East-Siberian Arctic Shelf: the
857 Dmitry Laptev Strait, Environ. Res. Lett., 5, 2010.
858 Nicolsky, D. J., Romanovsky, V. E., Romanovskii, N., Kholodov, A. L., Shakhova, N. E., and Semiletov,
859 I.: Modeling sub-sea permafrost in the East Siberian Arctic Shelf: The Laptev Sea region, J. Geophys.
860 Res., 117, F03028, 2012.
861 Nightingale, P. D., Malin, G., Law, C. S., Watson, A. J., Liss, P. S., Liddicoat, M. I., Boutin, J., and
862 Upstill-Goddard, R. C.: In situ evaluation of air-sea gas exchange parameterizations using novel
863 conservative and volatile tracers, Global Biogeochem. Cycles, 14, 373-387., 2000.
864 Nisbet, E. G., Dlugokencky, E. J., and Bousquet, P.: Methane on the Rise—Again, Science, 343, 493-495,
865 2014.
866 Pugach S.P., Pipko I.I., Semiletov I.P., Sergienko V.I.: Optical characteristics of the colored dissolved
867 organic matter on the East Siberian Arctic Shelf. Dokladi Earth Sciences, 465 (2), 1293-1296, 2015
868 (Translated from Russian to English by Springer)
869 Rehder, G., Keir, R. S., Suess, E., and Rhein, M.: Methane in the Northern Atlantic controlled by
870 microbial oxidation and atmospheric history, Geophys. Res. Lett., 26, 587-590, 1999.
871 Rehder, G., Leifer, I., Brewer, P. G., Friederich, G., and Peltzer, E. T.: Controls on methane bubble
872 dissolution inside and outside the hydrate stability field from open ocean field experiments and
873 numerical modeling, Mar. Chem., 114, 19-30, 2009.
874 Romanovskii, N. N., Hubberten, H.-W., Gavrilov, A. V., Eliseeva, A. A., and Tipenko, G. S.: Offshore
875 permafrost and gas hydrate stability zone on the shelf of East Siberian Seas, Geo-Mar. Lett., 25, 167-
876 182, 2005.
877 Schneider von Deimling, J., Greinert, J., Chapman N.R., Rabbel, W., and Linke, P.: Acoustic imaging of
878 natural gas seepage in the North Sea: Sensing bubbles controlled by variable currents, Limn.
879 Oceanog. Methods, 8, 155-171, 2010.
880 Schneider von Deimling, J., Rehder, G., Greinert, J., McGinnis, D. F., Boetius, A., and Linke, P.:
881 Quantification of seep-related methane gas emissions at Tommeliten, North Sea, Cont. Shelf Res., 31,
882 867-878, 2011.
883 Semiletov, I., Pipko, I., Gustafsson, Ö., Anderson, L. G., Sergienko, V., Pugach, S., Dudarev, O.,
884 Charkin, A., Gukov, A., Bröder, L., Andersson, A., Spivak, E. and Shakhova, N.: Acidification of
885 East Siberian Arctic Shelf waters through addition of freshwater and terrestrial carbon, Nature
886 Geosci., 9, 361–365, 2016.
887 Semiletov, I. P., Shakhova, N., Pipko, I. I., Pugach, S. P., Charkin, A. N., Dudarev, O. V., Kosmach, D.
888 A., and Nishino, A.: Space-time dynamics of carbon stocks and environmental parameters related to
889 carbon dioxide emissions in the Buor-Khaya Bay of the Laptev Sea, Biogeosci., 10, 5977-5996, 2013.
890 Semiletov, I. P., Shakhova, N. E., Sergienko, V. I., Pipko, I. I., and Dudarev, O. V.: On carbon transport
891 and fate in the East Siberian Arctic land-shelf-atmosphere system, Environ. Res. Lett., 7, 015201, doi:
892 10.1088/1748-9326/7/1/015201, 2012.
893 Serreze, K. C., Stroeve, J., Mauritzen, C., Cazenave, A., Rignot, E., Bates, N. R., Canadell, J. G.,
894 Raupach, M. R., Shakhova, N., and Semiletov, I.: Arctic climate feedbacks: Global implications,
895 World Wildlife Foundation, 98 pp., 2009.
896 Shakhova, N. and Semiletov, I.: Methane release and coastal environment in the East Siberian Arctic
897 Shelf, J. Mar. Sys., 66, 227-243, 2007.
898 Shakhova N.E., and Semiletov, I. P.: Methane hydrate feedbacks, In: Sommerkorn, M., and Hassol, S. J.,
899 eds., *Arctic Climate Feedbacks: Global Implications*, Published by WWF International Arctic
900 Programme August, 2009, ISBN: 978-2-88085-305-1, p. 81-92, 2009.
901 Shakhova, N. E., Sergienko, V. I., and Semiletov, I. P.: Modern state of the role of the East Siberian Shelf
902 in the methane cycle, Herald of the Russ. Acad. Sci., 79, 507-518, 2009a. (translated in English by
903 Springer)

The Cryosphere Discuss., doi:10.5194/tc-2016-156, 2016
Manuscript under review for journal The Cryosphere
Published: 7 July 2016

Shakhova, N., Nicolsky, D. J., and Semiletov, I. P.: On the current state of sub-sea permafrost in the East-Siberian Shelf testing of modeling results by observational data, Trans. Russ. Acad. Sci., 429, 2009b. (translated in English by Springer)

Shakhova N.E., Alexeev V.A., and Semiletov, I. P.: Accessing future increase in methane emission over the East-Siberian Shelf, Trans. Russ. Acad. Sci., 429, 4, 2009c (translated in English by Springer)

Shakhova, N., Semiletov, I., Leifer, I., Rekant, P., Salyuk, A., and Kosmach, D.: Geochemical and geophysical evidence of methane release over the East Siberian Arctic Shelf, J. Geophys. Res., 115, C08007, 2010a.

Shakhova, N., Semiletov, I., Salyuk, A., Iossoupov, V., Kosmach, D., and Gustafsson, O.: Extensive methane venting to the atmosphere from sediments of the East Siberian Arctic Shelf, Science, 327, 1246-1249, 2010b.

Shakhova, N., Semiletov Igor P., Leifer, I., Sergienko, V., Salyuk, A., Kosmach, D., Chernikh, D., Stubbs, C., Nicolsky, D., Tumskoy, V., and Gustafsson, O.: Ebullition and storm-induced methane release from the East Siberian Arctic Shelf, Nature Geosci., 7, 64-70, 2014.

Shakhova N., Semiletov, I., Sergienko, V., Lobkovsky, L., Yusupov, V., Salyuk, A., Salomatin, A., Chernykh, D., Kosmach, D., Panteleev, G., Nicolsky, D., Samarkin, V., Joye, S., Charkin, A., Dudarev, O., Meluzov, A., Gustafsson O.: The East Siberian Arctic Shelf: Towards further assessment of permafrost-related methane fluxes and role of sea ice. Phil. Trans. Royal Soc. A, 373: 20140451, 2015.

Solomon, E., Kastner, M., MacDonald, I. R., and Leifer, I.: Considerable methane fluxes to the atmosphere from hydrocarbon seeps in the Gulf of Mexico, Nature Geosci. 2, 561-565, 2009.

Soloviev, V. A., Ginzburg, G. D., Telepnev, E. V., and Mihalyuk, Y. N.: Cryothermia and natural gas hydrates within the Arctic Ocean, Sevmorgeologiya, Leningrad, 1987.

Stubbs, C.: Spatial distribution of near-shore gas seepage from sub-sea permafrost in the Laptev Sea Shelf, Arctic Ocean, MS, Geological Sciences, University of California, Santa Barbara, Santa Barbara, 118 pp., 2010.

Tarnocai, C., Canadell, J. G., Schuur, E. A. G., Kuhry, P., Mazhitova, G., and Zimov, S.: Soil organic carbon pools in the northern circumpolar permafrost region, Global Biogeochem. Cycles, 23, GB2023, 2009.

Tsuchiya, K., Ohsaki, K., and Taguchi, K.: Large and small bubble interaction patterns in a bubble column, Intnl. J. Multiphase Flow, 22, 121-132, 1996.

Warzinski, R. P., Lynn, R., Hasljasmaa, I., Leifer, I., Shaffer, F., Anderson, B. J., and Levine, J. S.: Dynamic morphology of gas hydrate on a methane bubble in water: Observations and new insights for hydrate film models, Geophys. Res. Lett., 41, 6841-6847, 2014.

Washburn, L., Clark, J. F., and Kyriakidis, P.: The spatial scales, distribution, and intensity of natural marine hydrocarbon seeps near Coal Oil Point, California, Mar. Petr. Geol., 22, 569-578, 2005.

Weber, T. C., Mayer, L., Jerram, K., Beaudoin, J., Rzhanov, Y., and Lovalvo, D.: Acoustic estimates of methane gas flux from the seabed in a 6000 km^2 region in the Northern Gulf of Mexico, Geochem., Geophys., Geosys., 15, 1911-1925, 2014.

Wilson, D., Leifer, I., and Maillard, E.: Megaplume bubble process visualization by 3D multibeam sonar mapping, J. Mar. Petr. Geol., 68, 753-765, 2015.

Wunch, D., Wennberg, P. O., Toon, G. C., Keppel-Aleks, G., and Yavin, Y. G.: Emissions of greenhouse gases from a North American megacity, Geophys. Res. Lett., 36, 2009.

The Cryosphere Discuss., doi:10.5194/tc-2016-156, 2016
Manuscript under review for journal The Cryosphere
Published: 7 July 2016

950 **Tables**

951 **Table 1.** Integrated depth-windowed methane flux estimates.

952 Designation	$Q_{m\text{-SBES}}$*	S$Q_{m\text{-SBES}}$	$Q_{m\text{-MBES}}$**	S$Q_{m\text{-MBES}}$	Area	*U*	S$Q_{m\text{-MBES}}$
953	(mmol/m^2/s)	(mmol/s)	(mmol//m^2/s)	(mmol/s)	(km^2)	(%)	(L/s)
954 Seep 1	0.22	3.78	0.33	5.56	0.017	32	0.14
955 Seep 2	0.59	41.16	0.61	42.73	0.070	3.7	1.07
956 Seep 3	0.26	3.96	0.33	4.88	0.015	19	0.12

957

958 Q is volume flux, Q_m is mass flux, U is uncertainty, where U=($Q_{m\text{-MBES}}$-$Q_{m\text{-SBES}}$)/$Q_{m\text{-MBES}}$

959 *SBES – Single Beam Echosounder, 65-70 m, depth window.

960 **MBES – Multibeam Echosounder, 65-70 m, depth window.

961

962 **Table 2.** Fit parameters for seep area flux occurrence.

963 Name	$Q_{m\text{-}1}$*	$Q_{m\text{-}2}$	a	b	R^2
964	(mmol/m^2/s)	(mmol/m^2/s)	(-)	(mmol/m^2/s)	
965 Seep Area 1	0.1	0.2	-19.53	6.648	0.836
966 Seep Area 2	0.1	0.3	-11.34	6.27	0.9228
967 Seep Area 3	0.1	0.2	-19.85	6.798	0.8258

968 Fit from $Q_{m\text{-}1}$ *to* $Q_{m\text{-}2}$, where Q_m is the mass flux rate

969

970